Numerical and experimental investigation of multifunctional high-efficiency anti-icing nickel-plated carbon fiber heating elements for wing-shaped composite airfoils

Won Tae Lee[b], Dong Jun Hong[c], Young Woo Nam[c, d+] and Rho Shin Myong[a, b+]

[a]Research Center for Aircraft Core Technology, Gyeongsang National University, 501 Jinjudaero, Jinju, Gyeongsangnam-do, 52828, South Korea

[b]School of Mechanical and Aerospace Engineering, Gyeongsang National University, 501 Jinjudaero, Jinju, Gyeongsangnam-do, 52828, South Korea

[c]Graduate School of Aerospace and Mechanical Engineering, Korea Aerospace University, 76, Hanggongdaehak-ro, Deogyang-gu, Goyang-si, Gyeonggi-do, South Korea

[d]Department of Smart Drone Engineering, Korea Aerospace University, 76, Hanggongdaehak-ro, Deogyang-gu, Goyang-si, Gyeonggi-do, South Korea

[+]Co-corresponding authors: Young Woo Nam (ywnam@kau.ac.kr) and Rho Shin Myong (myong@gnu.ac.kr)

[1]ABSTRACT

This study introduces wing-shaped composite airfoils integrated with high-efficiency, multifunctional anti-icing heating elements composed of nickel-plated carbon fiber. The anti-icing performance of these airfoils was evaluated through experiments

[1] **List of abbreviations:** IRT, icing research tunnel; IPS, ice protection system; IR, infrared; XRD, X-ray diffraction; XPS, X-ray photoelectron spectroscopy; FE-SEM, field-emission scanning electron microscopy; EDS, energy-dispersive X-ray spectroscopy; MVD, mean volume diameter; LWC, liquid water content; LED, light-emitting diode; DC, direct current; 3D, three-dimensional; CFD, computational fluid dynamics; SST, shear stress transport; RANS, Reynolds-averaged Navier–Stokes; AoA, angle of attack.

conducted in an Icing Research Tunnel (IRT) under representative glaze icing conditions. These results indicate that the nickel-plated carbon fiber exhibits an electrothermal conversion efficiency of 0.1 W/°C and a heating rate of 0.64 °C/s. In particular, icing wind tunnel tests conducted at a power density of 9.0 kW/m^2 demonstrated that the heating zone remained above the freezing point, thereby preventing ice accretion, while runback ice formed in the region corresponding to X/C ≈ 24–32% during a 300 s accretion period. The experimental results demonstrated high reliability and accuracy, showing a temperature difference of less than 0.5 °C compared to the surface temperature predicted by the multiphysics anti-icing simulation under identical conditions.

Keywords: Aircraft icing, Icing wind tunnel test, Ice protection system, Nickel-plated carbon fiber, Wing-shaped composites.

1. Introduction

Aircraft icing presents a serious safety hazard when supercooled water droplets in icing clouds impact the aircraft's exterior surfaces [1–4]. The accumulation of ice on critical components such as wings, rotor blades, propellers, and engine intakes can significantly impair aerodynamic performance and reduce propulsion efficiency [5]. Ice accumulation on leading edges and control surfaces increases surface roughness, resulting in higher aerodynamic drag. Simultaneously, the altered airfoil profile reduces lift, leading to flight instability and potential safety hazards [6–8]. Consequently, aviation regulations require the installation of an ice protection system (IPS) to ensure safe operations under specific icing conditions [9]. Modern aircraft increasingly employ carbon fiber because of its superior specific strength and stiffness compared to metals

[10,11].

Previous studies have used icing wind tunnel tests to assess the impact of icing on carbon fiber composite materials; the results have been summarized in Table 1. Recent studies have investigated the dynamic ice accretion process on composite airfoil models under various conditions through numerical simulations and experimental investigations [12–15]. The resulting deterioration in aerodynamic performance due to ice formation has been quantitatively assessed. Ice accumulation disrupts the airflow around the airfoil, leading to flow separation and the generation of unsteady vortex structures [16,17]. Furthermore, various IPS strategies for composite surfaces have been experimentally evaluated. Superhydrophobic coatings facilitate the removal of water droplets from the surface due to external natural forces, thereby mitigating ice accumulation and enhancing anti-icing effectiveness [18,19]. Structural vibration and impulse-based methods remove accumulated ice by inducing shear stresses that exceed the critical threshold through mechanical oscillations and impulse forces [20]. Electrothermal heating elements have been employed to maintain the wing surface above freezing temperatures to prevent ice formation or periodically deice the surface [21–25].

Most research focused on IPS utilizing electrothermal heating elements, owing to their precise digital control, high thermal efficiency, and robust structural stability [26,27]. However, using carbon fiber as a heating element is constrained by its turbostratic graphite structure, which results in high electrical resistance and low conductivity [28]. Recent studies have shown that carbon fiber modified with metal nanoparticles exhibits significantly enhanced electrothermal properties due to increased electrical and thermal conductivity [29]. Earlier research primarily focused on the dispersion of conductive nanoparticles within the resin matrix and their electromagnetic properties. In contrast, our approach involves directly coating carbon fibers with a nickel layer. The dispersion of nanoparticles often presents challenges, including particle agglomeration, increased resin viscosity, and non-uniform distribution. Furthermore, it involves a highly complex process, as the mechanical and electrical properties of the nanomaterials are susceptible to their dispersion state. The choice of electroless metal plating technique not only addresses the agglomerations issues but also improves the electrothermal properties [30–32]. Various conductive metal nanoparticles, such as silver, nickel, and copper, have been successfully plated onto different fiber surfaces through oxidation–reduction reactions in aqueous solutions, imparting specific electrical and thermal properties to the material [33–35]. Remarkably, during the plating process, nickel forms a passive layer that provides excellent corrosion and abrasion resistance. Additionally, its high conductivity further enhances the electrical and thermal performance of carbon fiber when applied through electroless plating.

For this reason, we investigated IPS utilizing electroless nickel-plated carbon fibers. This anti-icing method contrasts sharply with previous studies on anti-icing wind tunnel tests on IPS using composite structures with conventional resistive heating elements and embedded conductive material networks, as shown in Table 1. *Against this background, the objective of this study is to propose a composite airfoil incorporating electroless nickel-plated carbon fibers to achieve efficient heat transfer and to evaluate the functionality of the electrothermal IPS under glaze ice conditions using icing wind tunnel tests and multiphysics icing simulations.*

These elements exhibit excellent electrical and thermal properties, enabling high electrothermal conversion efficiency and superior heating performance. We experimentally evaluated the composite airfoil by observing the dynamic ice formation process and monitoring surface temperature changes under icing conditions. The experiments were conducted in the icing research tunnel at Iowa State University. Figure 1 shows the concept of the proposed composite airfoil. A high-resolution digital imaging system captured the dynamic process of ice attachment and anti-icing on the model surface. An infrared (IR) camera quantitatively measured the surface temperature distribution. Additionally, the electrothermal IPS for an aircraft wing structure has been validated through a multiphysics anti-icing simulation under identical conditions to the experimental setup, ensuring functional performance assessment and model reliability.

2. Materials and methods

2.1 Nickel-plated carbon fiber

First, electroless nickel plating was performed on pristine carbon fiber purchased from Minhu Composite Co. Ltd. (Korea) to evaluate its electrical properties. The microstructure and surface morphology of the samples were characterized using X-ray diffraction (XRD), X-ray photoelectron spectroscopy (XPS), and field-emission scanning electron microscopy (FE-SEM; SU5000, Hitachi, Japan). Figure 2(a) shows FE-SEM images that clearly reveal a nickel-plating layer on the carbon fiber surface. Energy-dispersive X-ray spectroscopy (EDS; Ultim Max40, Oxford, UK) further confirmed that nickel was absent in the pristine carbon fiber, while the nickel-plated sample exhibited a high nickel content of 75.98 wt% (both in weight percentage and atomic ratio), as detailed in Table 2 and Figure 2(b). Figure 2(c) shows the XPS results (Nexsa, Thermo Fisher Scientific, USA) for both pristine and nickel-plated carbon fibers. XPS, which analyzes photoelectron kinetic energy to determine atomic composition and electron coupling, showed no detectable Ni peaks for the pristine carbon fiber. In contrast, a prominent peak at 856.1 eV was observed for the nickel-plated sample, corresponding to nickel atoms distributed on the fiber surface. Further structural analysis was performed using X-ray diffraction (XRD; Ultima IV, Rigaku, Japan), as shown in Figure 2(d). While the pristine carbon fiber exhibited no distinct peaks, the nickel-plated sample displayed characteristic nickel diffraction peaks at 2θ values of 43.5°, 50.6°, and 74.3°.

2.2 Heating performance

The heating performance of the nickel-plated carbon fiber element was evaluated using samples measuring 40 mm × 40 mm. Copper foil with electrodes attached at 5 mm intervals on both ends was used, as shown in Figure 3(a). Temperature measurements were recorded with an IR camera (FLIR E76, 24°). Figure 3(b) shows thermal images of both the pristine and nickel-plated carbon fibers at room temperature. At an applied voltage of 1.5 V for 5 min, the maximum surface temperatures of the samples changed over time, reaching an equilibrium state as heat dissipation balanced the generated heat, a condition calculated using Joule's law [36,37]. Figure 3(c) compares the temperature profiles of the two samples. The nickel-plated carbon fiber achieved an equilibrium temperature of 85.6 ℃, 2.61 times higher than that of the pristine carbon fiber. Additionally, the heating rate of the nickel-plated sample reached 0.61 ℃/s at 100 s, which is 8.76 times faster compared to the pristine sample. To further assess its performance, the electrothermal conversion efficiency was determined using the following equation, with the corresponding values presented in Table 3:

$$h_{r+c} = \frac{I_c V_0}{T_m - T_0} \tag{1}$$

This equation confirms the effective heat-conversion characteristics of the nickel-plated carbon fiber, demonstrating its potential as a superior heating element. Its low resistance and high electrothermal conductivity contribute to its enhanced heating capacity. The heating mechanism is based on resistive heating, where the flow of electric current through the conductive medium results in electron movement and collisions with atomic nuclei. This process converts kinetic energy into thermal energy, allowing precise control of the generated heat by adjusting the applied voltage and current, independent of external conditions. According to Joule's law, the generated thermal energy (Q) can be expressed as follows:

$$V = IR \tag{2}$$

$$Q = I^2Rt \tag{3}$$

where V represents the voltage, I denotes the electric current, R denotes the resistance, and t denotes the duration of current flow. These equations quantify the thermal energy produced by current flowing through a resistive material, providing a basis for evaluating the enthalpy change and overall efficiency of the electrothermal heating system.

2.3 Experimental setup

This study was conducted in the multifunctional Icing Research Tunnel (IRT) at Iowa State University (ISU-IRT). Figure 4(a) presents a photograph of the actual test section, while Figure 4(b) illustrates a schematic of the experimental setup. The test section of the ISU-IRT measures 2.0 m in length, 0.4 m in width, and 0.4 m in height, and is enclosed by four optically transparent sidewalls to allow for visual observation during testing. A 30 hp fan/motor (Baldor™) propels the wind speed up to 60 m/s within the test section [38]. The tunnel is cooled by a heat exchanger, which is itself cooled by a 30 kW compressor (Vilter™), allowing the airflow temperature to drop to -25 °C. Under the set icing conditions, temperature fluctuations within the test section remain within ±1.0 °C [38]. Eight spray nozzles/atomizers (IKEUCHI BIMV 8002) are installed at the entrance of the tunnel contraction to inject micro-sized water droplets. Measurements using LaVision's ParticleMaster™ system confirmed that the droplets range from 10 to 100 μm, with a mean volume diameter (MVD) of approximately 20 μm under the test conditions [39]. The volumetric flow rate of water entering the tunnel is monitored using a digital flow meter (Omega, FLR-1605A). By adjusting the air pressure and water supply to the spray nozzles, the mass flow rate, and consequently the liquid water content (LWC), can be varied from 0.1 g/m^3 to 5.0 g/m^3 [40]. This flexibility enables the ISU-IRT to simulate a range of aircraft icing phenomena, from very dry rime ice (LWC ≈ 0.2 g/m^3) to wet glaze ice (LWC > 5.0 g/m^3).

For illumination during the icing experiments, a high-power light-emitting diode (LED) light unit (RPS Studio Light, Model RS-5620) provided low-flicker lighting. A high-resolution imaging system (PCO Tech PCO1200™ camera with a spatial resolution of 1248 × 1280 pixels) equipped with a 60 mm optical lens (Nikon, 60 mm Nikkor 2.8D) was positioned 50 mm above the airfoil model to record the ice formation and anti-icing processes [41].

Additionally, an IR thermal imaging system (FLIR-A615, spectral range 7.5–14 μm, resolution 640 × 640 pixels) mapped the temperature distribution on the airfoil surface during the anti-icing process. The IR camera was mounted approximately 300 mm above the airfoil, and the thermal radiation from the surface passed through an IR window (FLIR IR Window-IRW-4C, made of calcium fluoride) before reaching the camera [42]. During the experiments, the effect of the heating composite's thermal characteristics on aircraft icing was evaluated by applying power using a direct current (DC) power supply (Keysight, E36155A, 800W). Table 4 summarizes the test cases for the NACA0012 airfoil model equipped with a heating element under typical glaze ice accretion conditions. Glaze ice forms under relatively higher air temperatures, higher LWC, and larger MVD, especially under freezing drizzle conditions, compared to rime ice formation [43].

In these experiments, the incoming airflow velocity in the ISU-IRT was maintained at 40 m/s (V_∞), corresponding to a Reynolds number of approximately 600,000 based on the chord length of the test model. For the glaze icing tests, the ambient temperature and LWC of the incoming airflow were set at -5.0 °C and 0.5 g/m^3, respectively.

2.4 Numerical methods

The anti-icing simulation was performed using the CHT3D framework, which integrates key components from the advanced three-dimensional (3D) in-flight icing package, FENSAP-ICE. This approach combines multiple 3D computational domains, including viscous fluid dynamics, droplet collision dynamics, ice formation, and thermal conduction, to provide a detailed simulation of electrothermal anti-icing systems. Each module within FENSAP-ICE (covering airflow, droplet impact, ice formation, thermal conduction, and conjugate heat transfer) has been rigorously validated through experimental testing [44]. The computational fluid dynamics (CFD) module consists of three specialized solvers that manage airflow, droplet transport, and ice accretion with conjugate heat transfer.

Airflow is simulated using ANSYS-FLUENT, a compressible Navier–Stokes–Fourier solver based on the finite-volume method. This solver employs Roe's approximate Riemann solver, enhanced for high-order accuracy via the least squares method, and utilizes the k–omega shear stress transport (SST) turbulence model for the

Reynolds-averaged Navier–Stokes (RANS) equations, which improves the prediction of near-wall turbulence [45].

For the droplet phase, an Eulerian framework is used, incorporating additional continuity and momentum equations to resolve the partial differential equations governing droplet velocity and concentration. The complex three-dimensional droplet flow is handled by the DROP3D module in the FENSAP-ICE code [46], which provides distributions for collection efficiency and impingement limits on arbitrarily complex surfaces or within internal passages [47].

$$\begin{bmatrix} \rho \\ \rho\boldsymbol{u} \end{bmatrix}_t + \nabla \cdot \begin{bmatrix} \rho\boldsymbol{u} \\ \rho\boldsymbol{u}\boldsymbol{u} + \rho g d\boldsymbol{I} \end{bmatrix} = \begin{bmatrix} 0 \\ A_u(\boldsymbol{u}_a - \boldsymbol{u}) + \boldsymbol{S}_b + \nabla \cdot (\rho g d\boldsymbol{I}) \end{bmatrix} \tag{4}$$

The air and droplet velocity components are represented by $\boldsymbol{u}$ and $\boldsymbol{u}_a$, respectively. $\boldsymbol{S}_b$ is an estimation of the gravity and buoyancy forces on the droplet. The aerodynamic drag on droplets due to the airflow is represented by the term $A_u(\boldsymbol{u}_a - \boldsymbol{u})$. Finally, the term $\nabla \cdot (\rho g d\boldsymbol{I})$ is added to both sides of the momentum equation to resolve the non-strictly hyperbolic nature of the Eulerian droplet equations [8]. Computational models of atmospheric droplets fall into two categories, the clean airfield, and air-mixed droplet field. For this kind of flow, in general, the two-phase flow can further be simplified by ignoring the droplet effects on air flows. Since the mass loading ratio of the bulk density of the droplets over the bulk density of air is on the order of 10^{-3} in the air-droplet flow, the two-phase flow can be simulated using a weakly coupled (one-way coupling) algorithm. The air flow data should then be provided to the droplet solver through the source terms in the case of the Eulerian droplet equations.

The ice accretion solver employs conjugate heat transfer (CHT3D) to simulate ice thickness on the anti-icing surface. Here, the classical algebraic Messinger model is reformulated into partial differential equations governing mass balance and heat transfer at the surface to capture the complex ice geometries on wing structures [47]:

$$\rho_w \left[\frac{\partial h_f}{\partial t} + \nabla \cdot \left(\bar{\boldsymbol{u}}_f h_f\right)\right] = U_\infty LWC\beta - \dot{m}_{evap} - \dot{m}_{ice} \tag{5}$$

$$\begin{aligned} &\rho_w \left[\frac{\partial (h_f C_w \tilde{T})}{\partial t} + \nabla \cdot (\bar{\boldsymbol{u}}_f h_f C_w \tilde{T})\right] = \\ &\left[C_w \tilde{T}_{d,\infty} + \frac{|\mathbf{u}_d|^2}{2}\right] U_\infty LWC\beta - \frac{(L_{evap} + L_{subl})}{2}\dot{m}_{evap} + (L_{fusion} - C_{ice}\tilde{T})\dot{m}_{ice} \\ &\qquad + \varepsilon\sigma\left[{T_\infty}^4 - T^4\right] - C_h\left(\tilde{T} - \tilde{T}_{\infty 0}\right) + Q_{anti-icing} \end{aligned} \tag{6}$$

In these equations, the model estimates the instance mass of ice ($\dot{m}_{ice}$) and temperature at the wall/water/ice/air interface ($\tilde{T}$) along the surface. Unfrozen water is treated as runback water, and the velocity of the water film ($\bar{\boldsymbol{u}}_f$) is given by

$$\bar{u}_f(\mathrm{X}) = \frac{h_f}{2\mu_w}\tau_{wall}(\mathrm{X}) \tag{7}$$

Here, μ_w denotes the dynamic viscosity of water, h_f is the water film thickness, and τ_{wall} is the air wall shear stress. C_w, C_{ice}, and C_h represent the specific heats for water and ice and the convective heat transfer coefficient, respectively [4]. The term $\dot{m}_{evap}$ denotes the instantaneous mass rate of evaporated water, and L_{fusion}, L_{evap}, and L_{subl} represent the latent heats of fusion, evaporation, and sublimation, respectively. Additionally, T denotes temperature of air, T_∞ is the air temperature at infinity, $T_{\infty 0}$ is the stagnation temperature at infinity, $\tilde{T}_{d,\infty}$ is the droplet temperature, and u_d is the droplet velocity vector. The parameters ε and σ denote the solid emissivity and the Boltzmann constant, respectively [48,49]. The following compatibility conditions must also be satisfied:

$$h_f \geq 0, \qquad \dot{m}_{ice} \geq 0, \qquad h_f\tilde{T} \geq 0, \qquad \dot{m}_{ice}\tilde{T} \leq 0 \tag{8}$$

Heat conduction in the airfoil skin and heat generation from the IPS is implemented in a finite element formulation through the law of conservation of energy. In Equation (6), $Q_{anti-icing}$ represents the conjugate heat transfer arising from the thermal interaction between the solid and the fluid. Ice accretion in the presence of heat sources is governed by heat conduction, expressed as

$$\frac{\partial H_M(T)}{\partial t} = \nabla \cdot (k_M(T)\nabla T) + S_M(t) \tag{9}$$

where H_M and k_M denote the temperature-dependent enthalpy and thermal conductivity of the material M, respectively, T is the temperature, and S_M is a heat source term introduced to model the electric heaters. T denotes the solid material temperature, and t represents the time. The values of $\tilde{T}$ and T from Equations (5), (6), and (9) are used to compute $Q_{anti-icing}$:

$$Q_{anti-icing} = -Ak_M \frac{\partial T}{\partial \mathrm{n}} \tag{10}$$

where n is the normal vector, and A is the area of the boundary surface. In anti-icing simulations incorporating CHT, it is essential to resolve the mass, momentum, and energy conservation equations with temporal accuracy across multiple domains, including air and water flows, the water film, the ice layer, and the aircraft skin. The simulation begins with a steady-state airflow computation over the external domain, which serves as the baseline condition. Subsequently, water droplet impact is analyzed to quantify the mass accumulation on exposed surfaces. Newton iterations are carried out to ensure convergence of heat fluxes across the interfaces of all computational regions. Based on the resulting mass accumulation from the film and reduction due to melting, the evolving ice geometry is computed and subsequently re-meshed. The overall computational process is illustrated in Figure 5. The ice accretion analysis for wing-shaped composites with nickel-plated carbon fibers was conducted using ANSYS-FLUENT 2023 R1 and ANSYS FENSAP-ICE 2023 R1 (Ansys Inc., USA).

The numerical model replicates the dimensions used in the icing wind tunnel tests, comprising a chord length of 200 mm, a spanwise length of 400 mm, and a thickness of 2 mm, with no sweep angle or taper. Figure 6(a) depicts the numerical simulation domain and boundary conditions for the icing and multiphysics anti-icing simulation. In the simulation, velocity inlet and pressure outlet boundary conditions were applied to the external flow grid, while a prescribed heat flux was set on the solid grid to model the heating element at the leading edge of the wing-shaped composite. Wall boundary conditions were imposed on both the external flow and the solid surfaces. In addition to the initial mesh, finer and coarser meshes are also generated. This is done to investigate the grid dependency. Figure 6(b) shows the wall Y-plus chart around the NACA0012 airfoil surface. The initial cell height of all grids is set to 5×10^{-6} m, which satisfies $y+ \leq$

1. The far-field size and the extrusion rate remain the same, while the growth rate is adapted. A description of the grid setup is presented in Table 5. The initial grid comprised 82,368 cells in the external flow domain and 65,520 cells in the solid domain. Table 4 details the flow conditions used in the icing simulations, which were identical to those in the icing wind tunnel tests (i.e., an airflow speed of 40 m/s, a temperature of -5 ℃, an MVD of 20 μm, an LWC of 0.5 g/m^3, and an exposure time of 300 s). The simulations considered an airfoil angle of attack (AoA) of 0° and IPS heat flux values of 5 kW/m^2 and 9 kW/m^2.

3. Wing-shaped composite airfoils

3.1 Design and fabrication

As described in Sections 2.1 and 2.2, electroless nickel plating was applied to carbon fiber to enhance its electrical and thermal characteristics, yielding heating elements with superior electrothermal conversion efficiency. Figure 7(a) shows the lay-up sequence for the proposed wing-shaped composite, which incorporates these advanced heating elements. The structure consists of seven laminated layers with a total thickness (T_{total}) of 2.28 mm. At its core is a single ply of nickel-plated carbon fiber (0.15 mm thick) that serves as the heating element. This central layer is bordered by two plies of glass fiber/epoxy (each 0.36 mm thick) to provide essential electrical insulation and resistance bonding. On either side of this configuration, three plies of carbon fiber/epoxy (each 0.36 mm thick) are added to support load-bearing and facilitate thermal transfer. Finally, a ply of glass fiber/epoxy (0.18 mm thick) is applied to both the top and bottom surfaces of the heat sink, ensuring ignition protection and uniform thermal distribution. This arrangement is designed to optimize thermal transfer in the perpendicular direction. Figure 7(b) provides an overview of the fabrication process for the proposed wing-shaped composite airfoil. After the model lay-up was completed, the layered sample was vacuum-bagged and subjected to an autoclave curing cycle, which consisted of a 120 min dwell at 130 ℃ under a pressure of 7 atm. Once fully cured, the specimens were further prepared for the icing tunnel tests by applying an enamel spray coating and attaching an aluminum skin body.

3.2 Electrothermal heating performance

Before testing, a heating element layer was embedded along the entire leading edge of the wing-shaped composite. This setup was then mounted onto an aluminum fixture and evaluated at ambient temperature to verify its heating performance. The test system consisted of a DC power supply (E36154A, 800W, Keysight, USA) connected to the wing model and a recording host computer, as shown in Figure 8.

The heating rate and heat evolution were monitored using an IR camera as the voltage was varied, and the temperature distribution was quantitatively assessed from IR images of the heated area on the composite surface. Figure 9(a) shows the location of the heating element within the fabricated structure along with a schematic of the airfoil/wing configuration. The perspective view demonstrates that the heating element is embedded along the leading edge over a length of 400 mm. Room-temperature tests were conducted over 300 s at voltage levels of 6.0, 8.0, and 10 V. Figure 9(b) shows the corresponding temperature profiles and IR images. With increasing voltage, the maximum temperatures reached were 45.3, 65.1, and 92.4 ℃, respectively, while the corresponding heating rates up to 300 s were 0.07, 0.14, and 0.23 ℃/s, as shown in Figure 9(c). The power density applied over the heating element ranged from 1.43 kW/m^2 to 4.07 kW/m^2, indicating that power increases with higher voltage. Based on these results, the proposed heating elements demonstrate effective electrothermal performance. Table 6 presents the voltage, current, and power density for each test case. Several studies have examined the impact of highly conductive materials on electrothermal properties using various nanoparticle and hybrid filler formulations [50–60] to achieve optimal performance. The findings from this study suggest that nickel-plated carbon fiber holds significant potential for application in wing-shaped configurations.

4. Results and discussion

4.1 Droplet field analysis

The simulation quantitatively predicted the rate of droplets impacting the model surface during icing wind tunnel experiments. Figure 10 shows the distribution of LWC and collection efficiency around the airfoil for an LWC of 0.5 g/m^3 and an MVD of 20 μm. The LWC distribution is symmetrical, which is consistent with the NACA0012 airfoil's inherent symmetry, and it shows a concentrated accumulation at the leading edge under 0° AoA. Additionally, distinct shadow zones are observed at the top and bottom of the airfoil, beginning at X/C = 17% of the chord. The collection efficiency peaks at 0.8 when S/C = 0.030%, and it drops to nearly zero beyond S/C = 0.042%.

4.2 Characteristics of dynamic ice accretion process over the airfoil

The dynamic process of ice accretion and anti-icing was recorded to evaluate the impact of the heating composite's power density on the system's performance. Figure 11 presents icing wind tunnel test results for a model with a nickel-plated carbon fiber heating composite integrated into the leading edge of a NACA0012 airfoil under glaze icing conditions (U_∞ = 40 m/s, T_∞ = 268.15 K, LWC = 0.5 g/m^3). Before activating the water spray system in the ISU-IRT, the heating composite was energized for 5 min at power densities of P = 5.0 kW/m^2 and P = 9.0 kW/m^2. Figure 11(a) shows the test results at a power density of P = 5 kW/m^2 after 300 s of water spray. Supercooled water droplets impacted the front surface of the airfoil, where some droplets froze immediately upon contact with areas below the freezing point, leading to ice accretion along the leading edge. In contrast, droplets that struck regions above the freezing point remained liquid. Over time, the thickness of the ice on the leading edge increased gradually, reaching 4.81 mm by the end of the 300 s test. Liquid droplets that did not freeze were carried downstream by aerodynamic shear forces, transporting water away from the heating zone. In the cold inlet airflow (T_∞ = -5.0 ℃), as water moved out of the heating zone (X/C < 17%), it eventually froze, forming rivulet-shaped runback ice between X/C = 20% and X/C = 32% at t = 60 s. As the test continued, the length of the runback ice increased from X/C = 17% to X/C = 32% by t = 300 s.

Figure 11(b) presents the results at a higher power density of P = 9.0 kW/m^2. Under these conditions, the surface heating was sufficient to keep all impinging water droplets in a liquid state upon contact with the airfoil's leading edge, preventing immediate freezing. Instead, the droplets formed a thin water film with fine rivulets that were transported downstream. As the water exited the heating zone, the cold inlet airflow gradually cooled it, causing runback ice to form between X/C = 24% and X/C = 32% over 300 s. In this case, although the ice thickness within the affected section increased, the overall length of the runback ice was reduced compared to the lower power density test (5.0 kW/m^2). Specifically, the point at which the runback water froze was delayed by approximately X/C = 7%, and the overall length was reduced by approximately X/C = 9%. Simulation results closely matched the experimental observations.

Figure 12(a) shows that the simulated ice thickness on the leading edge differed by approximately 2 mm (approximately 1% of the chord) compared to experimental results, with the simulated runback ice length spanning X/C = 17% to X/C = 30% a range similar to that observed in the tests. Similarly, Figure 12(b) indicates that the simulation accurately predicted the increased liquid phase of droplets and the corresponding runback ice length at the front of the airfoil, with runback ice extending from X/C = 22% to X/C = 31%. Figure 12(c) shows the icing shapes around the NACA 0012 airfoil predicted by simulation. These findings validate the experimental results and confirm the effectiveness of the anti-icing system.

Figure 13 shows velocity contours and airflow streamlines for clean airfoils and airfoils of various power densities in an icing environment. Figure 13(b) shows the velocity distribution for the ice formation generated at a power density of P = 5 kW/m^2. Streamlined ice formation on the leading edge of an airfoil does not significantly change the aerodynamic velocity profile compared to a clean airfoil. Thin, long runback ice formed past the heating area causes localized flow acceleration and forms a separation bubble of size X/C = 0.005. Figure 13(c) shows the velocity distribution for the ice formation generated at a power density of P = 9 kW/m^2. The droplets that moved downstream while maintaining a liquid state at the airfoil leading edge generated relatively short and thick runback ice. This runback ice formed a separation bubble with a size of X/C = 0.05, causing flow separation. As a result, the drag coefficient for the case of P = 5 kW/m^2 is C_d = 0.0148, and for the case of P = 9 kW/m^2, it is C_d = 0.0400, which are 182% and 493% higher, respectively, compared to the drag coefficient of the clean airfoil, C_d = 0.0081.

4.3 Results of IR thermal imaging

The impact of nickel-plated carbon fibers on the anti-icing performance of the airfoil surface was quantitatively assessed using an IR imaging system. Figure 14 shows the surface temperature distributions at power densities of P = 5.0 kW/m^2 and P = 9.0 kW/m^2, along with time-dependent temperature profiles at four chordwise locations on the airfoil (X/C ≈ 0.1% at the leading edge, X/C ≈ 1.0% in the middle of the heated zone, X/C ≈ 10%, and X/C ≈ 20% near the end of the heated zone). Once the incoming airflow reached the set temperature and power was applied, supercooled droplet spraying began once the heated region achieved thermal stability. Figure 14(a) presents the IR imaging results at P = 5.0 kW/m^2. Prior to droplet spraying, the temperature distribution in the heating zone was lower near the leading edge owing to high convective heat transfer (e.g., T_w ≈ 0.40 °C at X/C ≈ 0.10% and T_w ≈ 2.0 °C at X/C ≈ 1.0%). The temperature then increased toward the center of the heated area (e.g., T_w ≈ 6.0 °C at X/C ≈ 10%) before decreasing in the downstream region (e.g., T_w ≈ 2.0 °C at X/C ≈ 20%). After activating the ISU-IRT's water spray system at t = 0 s, the surface temperature dropped rapidly as airborne supercooled droplets struck the airfoil. In the region near the leading edge, where the temperature was below freezing, droplets froze immediately upon impact. For t > 40 s, the temperature in the heating zone declined more moderately and eventually leveled off.

Figure 14(b) shows the IR imaging results at a power density of 9.0 kW/m^2. The time evolution of the surface temperature under this higher power density was similar to that observed at 5.0 kW/m^2, with some notable differences. Before droplet spraying, the temperature near the leading edge was T_w ≈ 2.0 °C at X/C ≈ 0.10% and T_w ≈ 6.0 °C at X/C ≈ 1.0%, increasing to T_w ≈ 14.0 °C at X/C ≈ 10% before dropping to T_w ≈ 8.0 °C at X/C ≈ 20%. After the water spray began, the temperature at the leading edge (X/C ≈ 0.10%) was ~1.0 °C higher than at the lower power density, which suggests that the impinging supercooled droplets remained in the liquid state as they passed through the heating area. At P = 9.0 kW/m^2, the entire heating zone maintained temperatures above the freezing point, ensuring a continuous "running wet" condition. The experimental surface temperature profiles were compared with multiphysics anti-icing simulation results for further validation.

Figure 15 presents the experimental data, extracted from seven points in the heating region (X/C < 17%), alongside the simulation results. At P = 5.0 kW/m^2, the average temperature difference was 0.43 ℃, while at P = 9.0 kW/m^2, it was 0.49 ℃. These differences, all below 0.50 ℃, highlight the reliability and accuracy of the experimental results

5. Conclusions

This paper presents wing-shaped composite airfoils equipped with high-efficiency, multifunctional anti-icing heating elements made from nickel-plated carbon fibers. These elements exhibit excellent electrical and thermal properties, enabling high electrothermal conversion efficiency and superior heating performance. Our tests revealed that increasing the plating thickness and the weight percentage of nickel particles significantly enhances performance, resulting in an electrothermal conversion efficiency of 0.1 W/℃ and a heating rate 8.76 times greater than that of pristine carbon fiber. Electrothermal tests of the wing-shaped composite airfoil demonstrated that, at 10.0 V and a power density of 4.66 kW/m^2, the surface temperature reached 92.4 ℃. Additionally, an experimental investigation in the ISU-IRT evaluated the anti-icing performance under dynamic glaze icing conditions. The results indicated that a power density of 9.0 kW/m^2 enabled complete anti-icing functionality, as the nickel-plated carbon fiber heating element effectively prevented ice formation along the leading edge. Notably, supercooled water droplets remained in the liquid phase upon impingement, and the water was subsequently carried downstream by the incoming airflow, forming runback ice in the region between X/C = 24% and X/C = 32%. These experimental results were consistent with multiphysics anti-icing simulations performed under the same conditions. Overall, the results demonstrate that nickel-plated carbon fiber heating elements exhibit multifunctional properties and can serve as an efficient solution for practical aerospace anti-icing systems. To enhance performance and mitigate runback ice formation observed during wind tunnel testing, superhydrophobic coatings will be incorporated in future detailed experiments, contributing to improved scalability and practical deployment in aerospace applications.

Acknowledgments

This research was supported by the National Research Foundation of Korea (NRF) funded by the Ministry of Science and ICT, Republic of Korea (No. RS-2024-00397400)

References

[1] Esmaeilifar E, Prince Raj L, Myong RS. In-flight Anti-icing Simulation of Electrothermal Ice Protection Systems with Inhomogeneous Thermal Boundary Condition. Aerospace Science and Technology 2024;150:109210. https://doi.org/10.1016/j.ast.2024.109210.

[2] Raj LP, Prince Raj L, Yee K, Myong RS. Sensitivity of Ice Accretion and Aerodynamic Performance Degradation to Critical Physical and Modeling Parameters Affecting Airfoil Icing. Aerospace Science and Technology 2020;98:105659. https://doi.org/10.1016/j.compositesb.2019.01.045.

[3] Roy R, Raj LP, Jo JH, Cho MY, Kweon JH, Myong RS. Multiphysics Anti-icing Simulation of a CFRP Composite Wing Structure Embedded with Thin Etched-foil Electrothermal Heating Films in Glaze Ice Conditions. Composite Structures 2021;276:114441. https://doi.org/10.1016/j.compstruct.2021.114441.

[4] Sen Gupta B, Raj LP, Cho MY, Son C, Yoon T, Yee K, Myong RS. Computational simulation of ice accretion and shedding trajectory of a rotorcraft in forward flight with strong rotor wakes. Aerospace Science and Technology

2021;119:107140. https://doi.org/10.1016/j.ast.2021.107140.
[5] Zhao G, Zhao Q, Chen X. New 3-D ice accretion method of hovering rotor including effects of centrifugal force. Aerospace Science and Technology 2016;48:122–130. https://doi.org/10.1016/j.ast.2015.10.018.
[6] Jung S, Raj LP, Rahimi A, Jeong HJ, Myong RS. Performance evaluation of electrothermal anti-icing systems for a rotorcraft engine air intake using a meta model. Aerospace Science and Technology 2020;106:106174. https://doi.org/10.1016/j.ast.2020.106174.
[7] Lee YM, Lee JH, Raj LP, Jo JH, Myong RS. Large-eddy simulations of complex aerodynamic flows over multi-element iced airfoils. Aerospace Science and Technology 2021;109:106417. https://doi.org/10.1016/j.ast.2020.106417.
[8] Raj LP, Lee JW, Myong RS. Ice accretion and aerodynamic effects on a multi-element airfoil under SLD icing conditions. Aerospace Science and Technology 2019;85:320–333. https://doi.org/10.1016/j.ast.2018.12.017.
[9] Federal Aviation Regulations Part 25: Airworthiness Standards: Transport Category Airplanes. 2015.
[10] Zheng X, Kim S, Park CW. Enhancement of thermal conductivity of carbon fiber-reinforced polymer composite with copper and boron nitride particles. Compos A 2019;121:449–456. https://doi.org/10.1016/j.compositesa.2019.03.030.
[11] Yao X, Hawkins SC, Falzon BG. An advanced anti-icing/de-icing system utilizing highly aligned carbon nanotube webs. Carbon N Y 2018;136:130–138. https://doi.org/10.1016/J.CARBON.2018.04.039.
[12] Gao L, Liu Y, Hu H. An experimental investigation of dynamic ice accretion process on a wind turbine airfoil model considering various icing conditions. Int J Heat Mass Transf 2019;133:930–939. https://doi.org/10.1016/j.ijheatmasstransfer.2018.12.181.
[13] Jasinski WJ, Noe SC, Selig MS, Bragg MB. Wind turbine performance under icing conditions. J Sol Energy Eng 1998;120:60–65. https://doi.org/10.1115/1.2888048.
[14] Wang C, Lin W, Lin X, Wu T, Meng Z, Cai A, Xu Z, Li Y, Feng F. The influence of angle of attack on the icing distribution characteristics of DU97 blade airfoil surface for wind turbines. Coatings 2024;14:160. https://doi.org/10.3390/coatings14020160.
[15] Lin W, Lin X, Wang C, Wu T, Meng Z, Cai A, Shen H, Li Y, Feng F. Wind tunnel tests of surface icing distribution on aluminum alloy and carbon fiber-reinforced polymer blades for wind turbines. Coatings 2023;13:810. https://doi.org/10.3390/coatings13050810.

[16] Yan S, Opazo TI, Palacios J, Langelaan JW, Germain LD. Experimental evaluation of multi-rotor UAV operation under icing conditions. In: Annual Forum Proceedings-AHS International 2018;1–12. https://doi.org/10.4050/F-0074-2018-12902.
[17] Gao L, Liu Y, Zhou W, Hu H. An experimental study on the aerodynamic performance degradation of a wind turbine blade model induced by ice accretion process. Renew Energy 2019;133:663–675. https://doi.org/10.1016/j.renene.2018.10.032.
[18] Wang S, Chang S, Qi H, Zhao H. Experimental study of icing and deicing situations of different wettability surfaces composite electric heating. Appl Therm Eng 2024;238:122045. https://doi.org/10.1016/j.applthermaleng.2023.122045.
[19] Liu B, Liu Z, Li Y, Feng F. A wind tunnel test of the anti-icing properties of MoS2/ZnO hydrophobic nano-coatings for wind turbine blades. Coatings 2023;13:686. https://doi.org/10.3390/coatings13040686.
[20] Endres M, Sommerwerk H, Mendig C, Sinapius M, Horst P. Experimental study of two electro-mechanical de-icing systems applied on a wing section tested in an icing wind tunnel. CEAS Aeronaut J 2017;8:429–439. https://doi.org/10.1007/s13272-017-0249-0.
[21] Müller NC, Løw-Hansen B, Borup KT, Hann R. UAV icing: Development of an ice protection system for the propeller of a small UAV. Cold Reg Sci Technol 2023;213:103938. https://doi.org/10.1016/j.coldregions.2023.103938.
[22] Karpen N, Diebald S, Dezitter F, Bonaccurso E. Propeller-integrated airfoil heater system for small multirotor drones in icing environments: Anti-icing feasibility study. Cold Reg Sci Technol 2022;201:103616. https://doi.org/10.1016/j.coldregions.2022.103616.
[23] Wallisch J, Hann R. UAV icing: Experimental investigation of ice shedding times with an electrothermal de-icing system. AIAA AVIATION 2022 Forum 2022. https://doi.org/10.2514/6.2022-3905.
[24] Mohseni M, Amirfazli A. A novel electro-thermal anti-icing system for fiber-reinforced polymer composite airfoils. Cold Reg Sci Technol 2013;87:47–58. https://doi.org/10.1016/j.coldregions.2012.12.003.
[25] Hasan MZ. Experimental and numerical analysis of anti-icing a GLARE laminate. Int J Thermofluids 2021;10:100087. https://doi.org/10.1016/j.ijft.2021.100087.
[26] Shinkafi A, Lawson C. Enhanced method of conceptual sizing of aircraft electrothermal de-icing system. Int J Aerospace Mech Eng 2014;8:1073–1080.
[27] Ding L, Chang S. Evaluation of inflight deicing performance for designed

electrothermal systems with experimental verification. J Aircr 2020;57:156–166. https://doi.org/10.2514/1.C035524.
[28] Das TK, Ghosh P, Das NC. Preparation, development, outcomes, and application versatility of carbon fiber-based polymer composites: A review. Adv Compos Hybrid Mater 2019;2:214–233. https://doi.org/10.1007/s42114-018-0072-z.
[29] Cao Y, Farha FI, Ge D, Liu X, Liu W, Li G, Zhang T, Xu F. Highly effective E-heating performance of nickel coated carbon fiber and its composites for de-icing application. Compos Struct 2019;229:111397. https://doi.org/10.1016/j.compstruct.2019.111397.
[30] Lee JS, Jo HS, Choe HS, Lee DS, Jeong HJ, Lee HR, Kweon JW, Lee H, Myong RS, Nam YW. Electro-thermal heating element with a nickel-plated carbon fabric for the leading edge of a wing-shaped composite application. Composite Structures 2022;289:115510. https://doi.org/10.1016/j.compstruct.2022.115510.
[31] Lee JS, Hoang VT, Kweon JH, Nam YW. Multifunctional Ni-plated carbon fiber reinforced thermoplastic composite with excellent electrothermal and superhydrophobic properties using MWCNTs and SiO_2/Ag microspheres. Composites Part A: Applied Science and Manufacturing 2023;171:107585. https://doi.org/10.1016/j.compositesa.2023.107585.
[32] Nam YW, Choi JH, Lee WJ, Kim CG. Fabrication of a thin and lightweight microwave absorber containing Ni-coated glass fibers by electroless plating. Composites Science and Technology 2017;145:165–172. https://doi.org/10.1016/j.compscitech.2017.04.009.
[33] Yu D, Mu S, Liu L, Wang W. Preparation of electroless silver plating on aramid fiber with good conductivity and adhesion strength. Colloids Surf A 2015;483:53–59. https://doi.org/10.1016/J.COLSURFA.2015.07.021.
[34] Xu C, Liu G, Chen H, Zhou R, Liu Y. Fabrication of conductive copper-coated glass fibers through electroless plating process. J Mater Sci Mater Electron 2014;25:2611–2617. https://doi.org/10.1007/s10854-014-1919-x.
[35] Choe HS, Lee JS, Nam YW, Lee JH, Kweon JH. The impact resistance and damage behavior of Ni-plated carbon fabric reinforced thermoplastic composites with embedded Cu mesh. Composite Structures 2021;279:115138. https://doi.org/10.1016/j.compstruct.2021.115138.
[36] Salim MU, Nishat FM, Oh T, Yoo DY, Song Y, Ozbakkaloglu T, Yeon JH. Electrical resistivity and joule heating characteristics of cementitious composites incorporating multi-walled carbon nanotubes and carbon fibers. Materials (Basel) 2022;15:8055. https://doi.org/10.3390/ma15228055.

[37] Liu S, Yang J, Yu Y, Liang D, Li Y, Si X, Song S, Meng M, Zhang J, Zhang Y. Multifunctional flexible carbon fiber felt@nickel composite films with core–shell heterostructure: Exceptional Joule heating capability, thermal management, and electromagnetic interference shielding. Chem Eng J 2024;494:153221. https://doi.org/10.1016/J.CEJ.2024.153221.
[38] H. Hu, L. Tian, C. Eluchie, H. Sista, H. Hu. A comparative study of using superhydrophobic and icephobic surface coatings for aircraft icing mitigation. AIAA Journal 2024;62(4):1588–1600. https://doi.org/10.2514/1.J063579.[39]
[39] Tian L, Hu H, Veerakumar R, Hu H. Ice accretion characteristics on rotating aeroengine fan blades. Exp Therm Fluid Sci 2024;155:111181. https://doi.org/10.1016/j.expthermflusci.2024.111181.
[40] Li L, Liu Y, Tian L, Hu H, Hu H, Liu X, Hogate I, Kohli A. An experimental study on a hot-air-based anti-/de-icing system for aero-engine inlet guide vanes. Appl Therm Eng 2020;167:114778. https://doi.org/10.1016/j.applthermaleng.2019.114778.
[41] Zhang Z, A L, Hu H, Bai X, Hu H. An experimental study on the detrimental effects of deicing fluids on the performance of icephobic coatings for aircraft icing mitigation. Aerospace Science and Technology 2021;119:1070909. https://doi.org/10.1016/j.ast.2021.107090.
[42] Liu Y, Zhang K, Tian W, Hu H. An experimental investigation on the dynamic ice accretion and unsteady heat transfer over an airfoil surface with embedded initial ice roughness. Int J Heat Mass Transf 2020;146:118900. https://doi.org/10.1016/j.ijheatmasstransfer.2019.118900.
[43] Gao L, Liu Y, Hu H. An experimental investigation on the dynamic glaze ice accretion process over a wind turbine airfoil surface. Int J Heat Mass Transf 2020;149:119120. https://doi.org/10.1016/j.ijheatmasstransfer.2019.119120.
[44] Wang H, Tran P, Habashi WG, Chen Y, Zhang M, Feng L. Anti-icing simulation in wet air of a piccolo system using FENSAP-ICE. J Aerosp 2007;116:715–723. https://doi.org/10.4271/2007-01-3357.
[45] Hellsten A, Laine S. Extension of the k-ω-SST turbulence model for flows over rough surfaces. 22nd Atmospheric Flight Mechanics Conference 1997:252–260. https://doi.org/10.2514/6.1997-3577.
[46] Bourgault Y, Boutanios Z, Habashi WG. Three-dimensional Eulerian approach to droplet impingement simulation using FENSAP-ICE, Part 1: Model, algorithm, and validation. J Aircr 2000;37:95–103. https://doi.org/10.2514/2.2566.
[47] Ahn GB, Jung KY, Myong RS, Shin HB, Habashi WG. Numerical and experimental investigation of ice accretion on rotorcraft engine air intake. J Aircr

2015;52:903–909. https://doi.org/10.2514/1.C032839.
[48] Beaugendre H, Morency F, Habashi WG. FENSAP-ICE's three-dimensional in-flight ice accretion module: ICE3D. J Aircr 2003;40:239–247. https://doi.org/10.2514/2.3113.
[49] Messinger BL. Equilibrium temperature of an unheated icing surface as a function of air speed. J Aeronaut Sci 1953;20:29–42. https://doi.org/10.2514/8.2520.
[50] Kang SI, Son SM, Heo SJ, Seong DG. Investigation on the optimized curing cycle of epoxy resin for enhancing thermal and mechanical properties of glass fiber reinforced plastic applications. Functional Composites and Structures. 2025;7(1):015007. 10.1088/2631-6331/adb005
[51] Wen X, Chen W, Chen K, Wang G, Shen C, Zhang J. Study on the electromagnetic wave absorption performance of dual-loss type composite MWCNT/CIP/GF/EP. Functional Composites and Structures. 2024;6(4):045004. 10.1088/2631-6331/ad88e5
[52] Jitianu A, Cacciaguerra T, Benoit R, Delpeux S, Béguin F, Bonnamy S. Synthesis and characterization of carbon nanotubes-TiO2 nanocomposites. Carbon 2004;42:1147–1151. https://doi.org/10.1016/J.CARBON.2003.12.041.
[53] Kumar K, Das S, Garg R, Goyat MS. A comprehensive review on enhancing the strength of CFRPs through nano-reinforcements: Applications, characterization, and challenges. J Fail Anal Prev 2024;24:1588–1627. https://doi.org/10.1007/S11668-024-01946-2.
[54] Choi BK, Choi WK, Seo MK. Effect of catalytic graphitization on the electric heating performance of electroless nickel-coated carbon fibers. Curr Appl Phys 2022;42:86–91. https://doi.org/10.1016/J.CAP.2022.08.003.
[55] Xu C, Duan G, Xu W, Wang X, Hu Y, Zhang X, Zhao H, Wang BX. Thermally tunable vanadium-dioxide-based broadband metamaterial absorber with switchable functionality in the terahertz band. Functional Composites and Structures. 2023;5(2):025004. 10.1088/2631-6331/acd490
[56] Fal M, Meinders R, Okanmisope F, Chandrashekhara K, Alabdulmuhsin A, Alotaibi A, Alqahtani S. Experimental and numerical study of increased core surface area on the performance of additively manufactured honeycomb sandwich structures. Functional Composites and Structures. 2024;6(2):025008. 10.1088/2631-6331/ad46de
[57] Ma Y, Guo L, Qi L, Sun J, Wang J, Cao Y. Growth mechanism and thermal behavior of electroless Cu plating on short carbon fibers. Surf Coat Technol 2021;419:127294. https://doi.org/10.1016/J.SURFCOAT.2021.127294.
[58] Li W, Zhou Y, Liu H, Yang J, Pei K. Improved strength, toughness and electrical

properties of rigid polyurethane composites reinforced with Ni-coated carbon fibers. Polym Bull 2022;79:5235–5245. https://doi.org/10.1007/S00289-021-03771-1.
[59] Pang J, Qin W, You W, Zhong M, Meng Q. Induction heating characteristics of electroless Ni-coated CFRP for deicing and anti-icing. Coatings 2023;13:1531. https://doi.org/10.3390/coatings13091531.
[60] Guo X, Yang Q, Zheng H, Dong W. Integrated composite electrothermal de-icing system based on ultra-thin flexible heating film. Appl Therm Eng 2024;236:121723. https://doi.org/10.1016/J.APPLTHERMALENG.2023.121723.

Figure Captions

Figure 1. Schematic of the ISU-IRT and the proposed wing-shaped composite airfoil.

Figure 2. (a) SEM images of the pristine carbon fiber and Ni-plated carbon fiber; (b) Ni-element (wt. %) EDS analysis results for nickel-plated carbon fabric; (c) XPS curves and XRD patterns.

Figure 3. (a) Electric heating test setup; (b) temperature distribution images (obtained via IR camera) of pristine and Ni-plated carbon fabric; (c) temperature profiles at an applied voltage of 1.5 V.

Figure 4. (a) Configuration image of the ISU-IRT test section; (b) Schematic of the experimental setup.

Figure 5. Flowchart of the multiphysics anti-icing simulation.

Figure 6. (a) Computational domain of a multiphysics icing simulation model comprising a solid and fluid grid; (b) The wall Y-plus around the NACA0012 airfoil surface.

Figure 7. (a) Configuration and lay-up sequence of the proposed wing-shaped composite airfoil with an integrated heating element along the leading edge; (b) fabrication process flow for the proposed wing-shaped composite airfoil.

Figure 8. Surface temperature measurement test setup for heating wing-shaped composite materials.

Figure 9. (a) 3D profile of the wing-shaped composite; (b) IR images of the composite at different applied voltages; (c) temperature profiles at various voltage levels.

Figure 10. LWC distribution (left) and collection efficiency (right) around a NACA0012 airfoil.

Figure 11. Time sequences of images capturing the anti-icing process on the wing-shaped composite at different power densities: (a) test case with U_∞ = 40 m/s, LWC = 1.0 g/m^3,

T_∞ = 268.15 K, and power density = 5 kW/m^2; (b) test case with U_∞ = 40 m/s, LWC = 1.0 g/m^3, T_∞ = 268.15 K, and power density = 9 kW/m^2.

Figure 12. Comparison of snapshots and computational analysis results of the ice formation process on the airfoil surface under power densities of (a) 5 kW/m^2 and (b) 9 kW/m^2, for test conditions of U_∞ = 40 m/s, LWC = 1.0 g/m^3, and T_∞ = 268.15 K; (c) Comparison between the shape of the ice on the wing during each case.

Figure 13. Velocity contour and airflow streamline of the airfoil at different power densities at (a) clean airfoil; (b) 5.0 kW/m^2 and (c) 9.0 kW/m^2.

Figure 14. Acquired IR thermal imaging results and time evolution of surface temperature during anti-icing tests at (a) 5.0 kW/m^2 and (b) 9.0 kW/m^2 under test conditions of U_∞ = 40 m/s, LWC = 1.0 g/m^3, and T_∞ = 268.15 K.

Figure 15. Comparison of the extracted surface temperature profile and simulation results at 300 s.

Figures

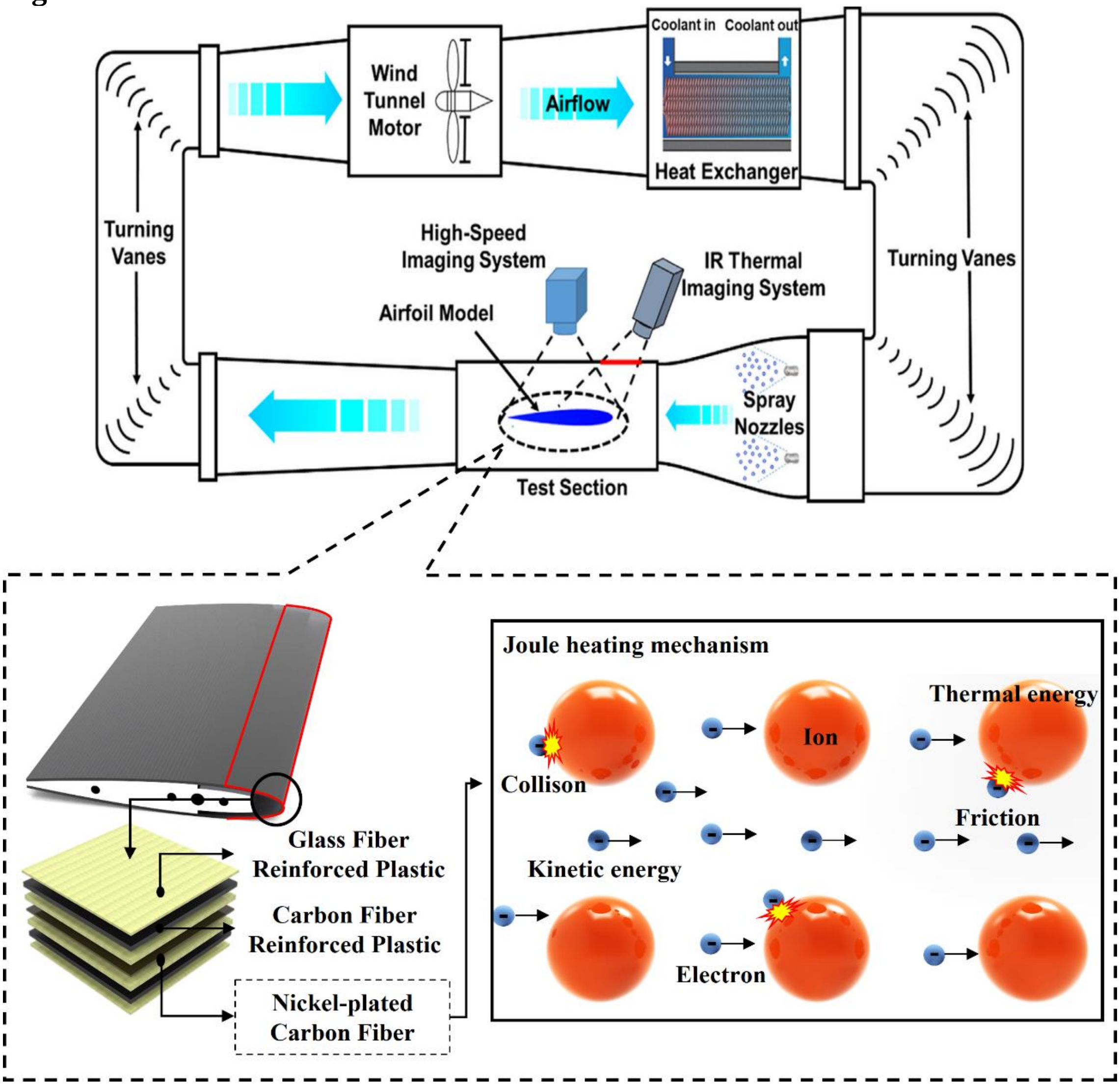

Figure 1

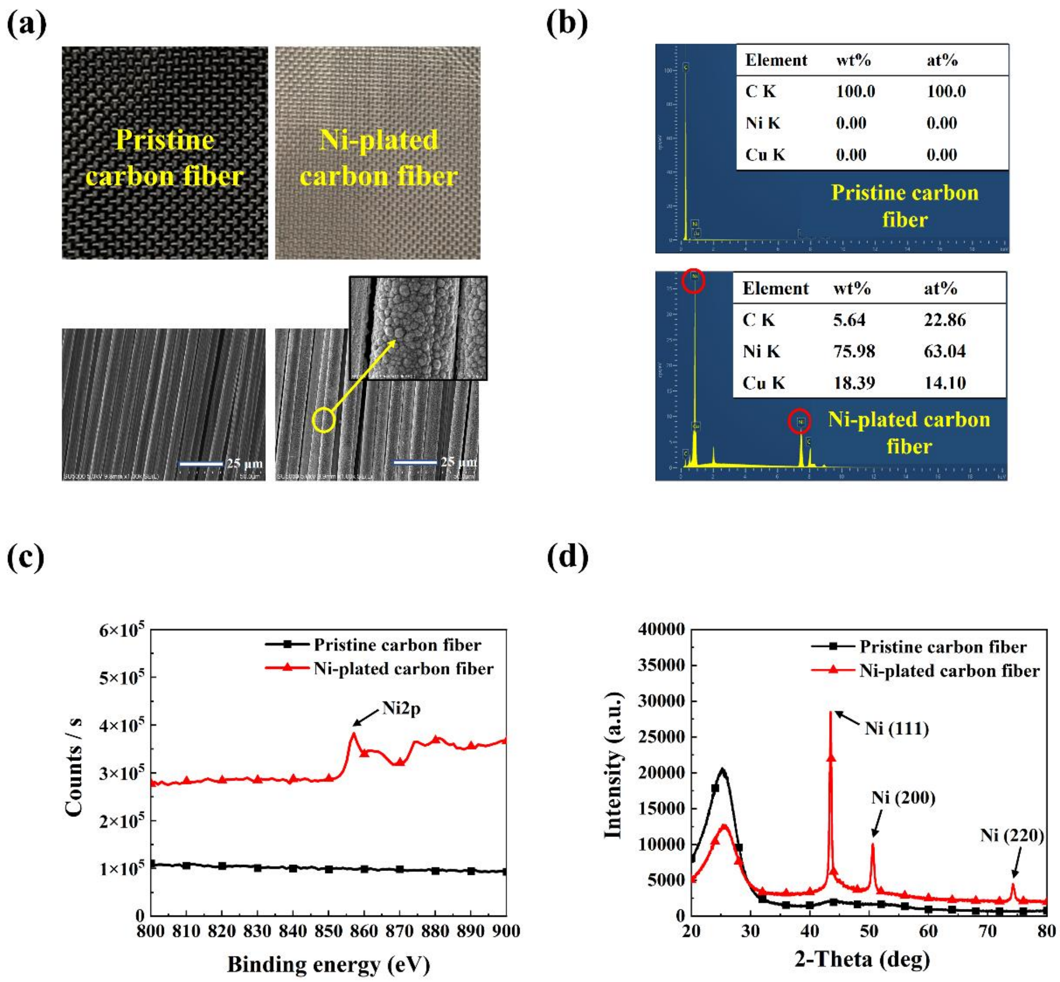
(a)
Pristine carbon fiber
Ni-plated carbon fiber
25 μm
25 μm
(b)
Element wt% at%
C K 100.0 100.0
Ni K 0.00 0.00
Cu K 0.00 0.00
Pristine carbon fiber
Element wt% at%
C K 5.64 22.86
Ni K 75.98 63.04
Cu K 18.39 14.10
Ni-plated carbon fiber
(c)
Pristine carbon fiber
Ni-plated carbon fiber
Ni2p
Counts / s
Binding energy (eV)
(d)
Pristine carbon fiber
Ni-plated carbon fiber
Ni (111)
Ni (200)
Ni (220)
Intensity (a.u.)
2-Theta (deg)

Figure 2

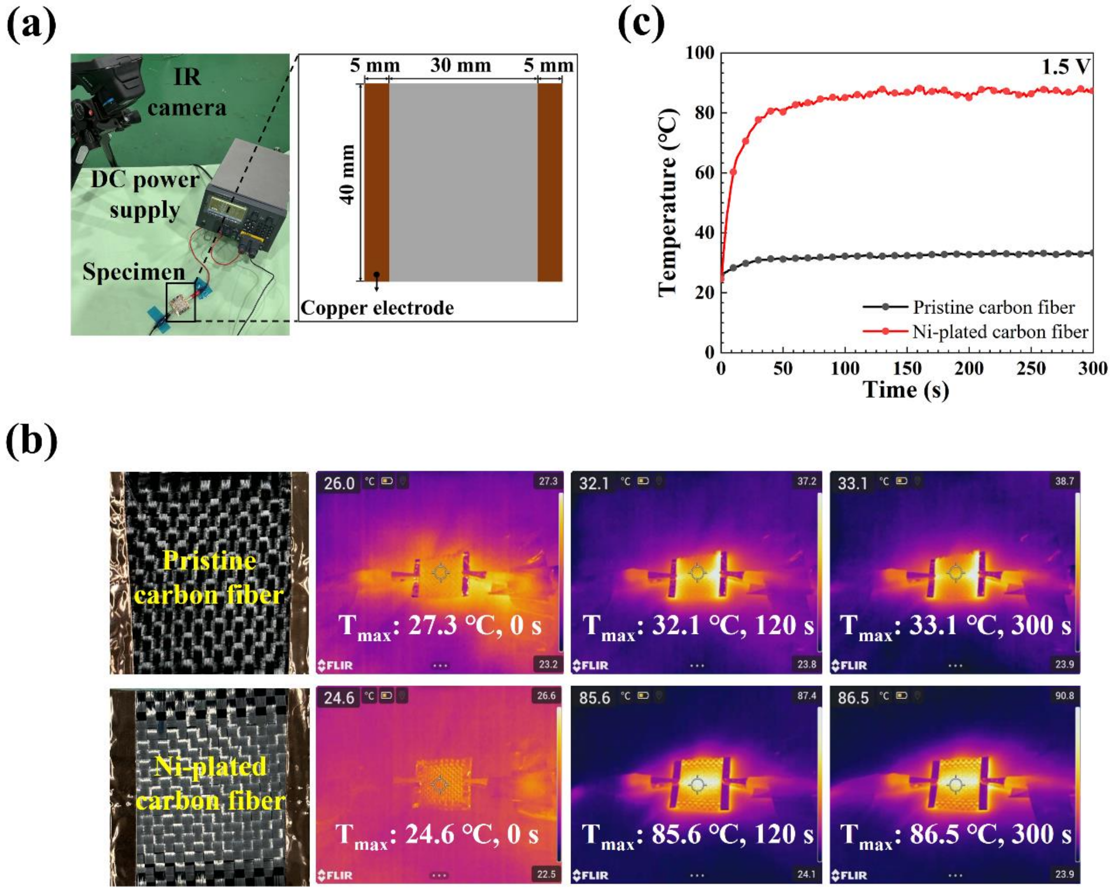
(a)
IR camera
DC power supply
Specimen
5 mm
30 mm
5 mm
40 mm
Copper electrode
(c)
1.5 V
Temperature (°C)
Time (s)
Pristine carbon fiber
Ni-plated carbon fiber
(b)
Pristine carbon fiber
Ni-plated carbon fiber
Tmax: 27.3 °C, 0 s
Tmax: 32.1 °C, 120 s
Tmax: 33.1 °C, 300 s
Tmax: 24.6 °C, 0 s
Tmax: 85.6 °C, 120 s
Tmax: 86.5 °C, 300 s

Figure 3

(a)

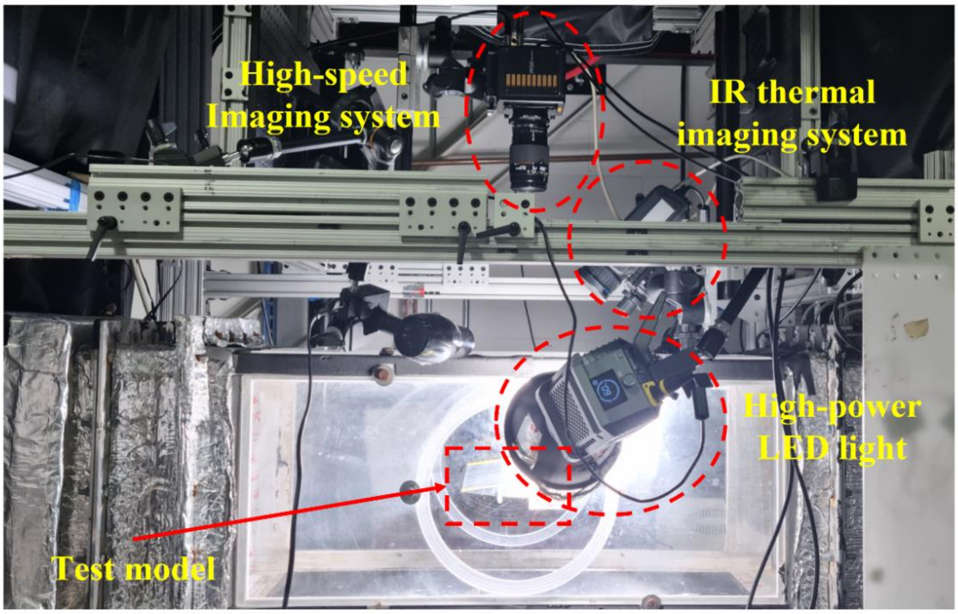
High-speed
Imaging system
IR thermal
imaging system
High-power
LED light
Test model

(b)

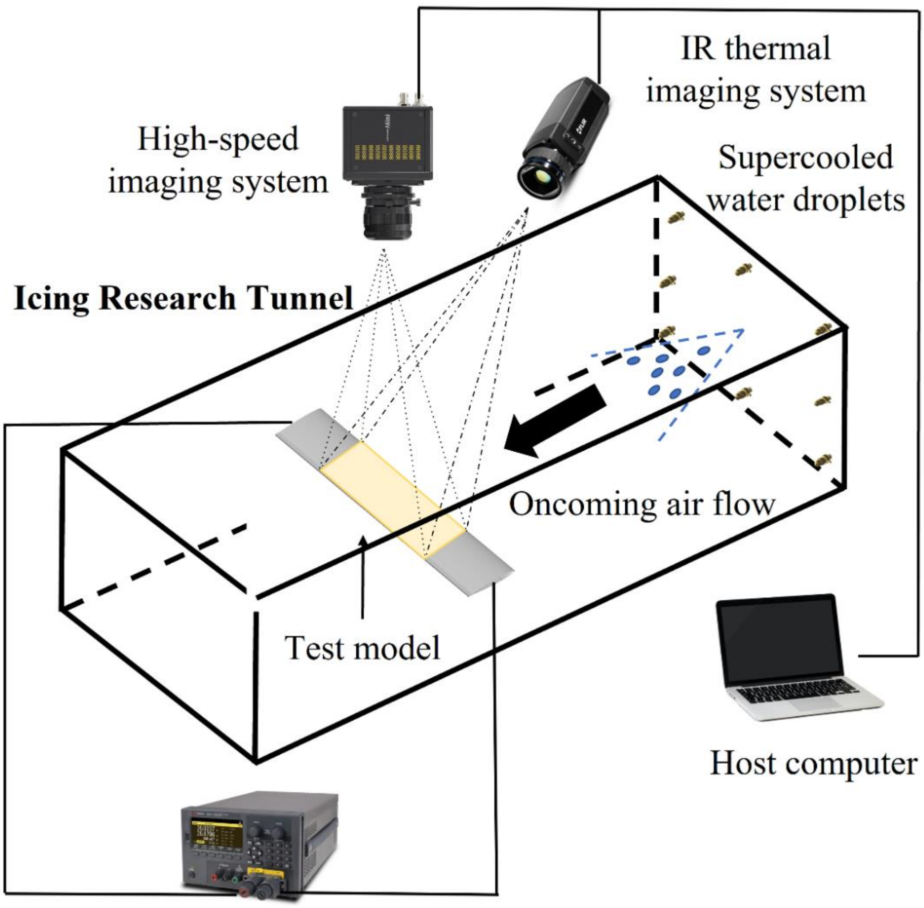
IR thermal
imaging system
High-speed
imaging system
Supercooled
water droplets
Icing Research Tunnel
Oncoming air flow
Test model
Host computer

Figure 4

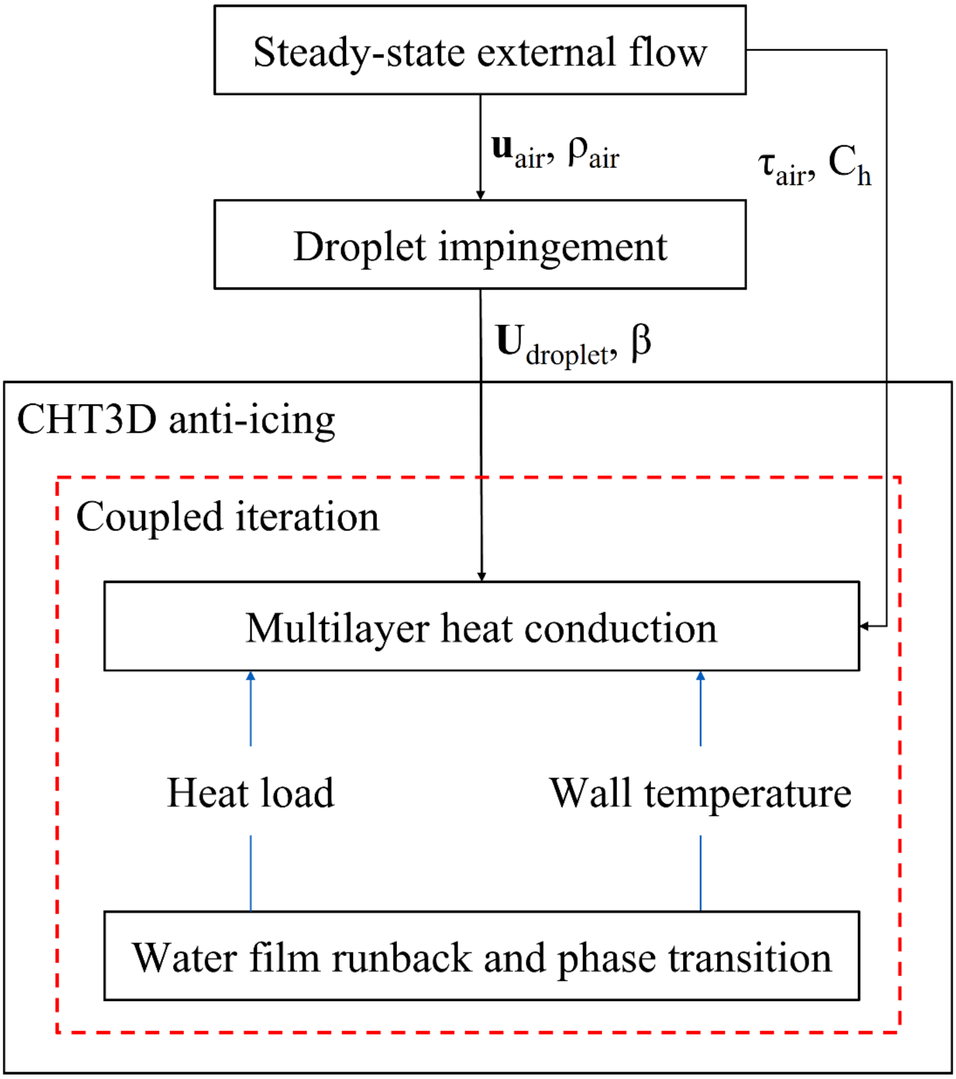
Steady-state external flow
$\mathbf{u}_{air}$, ρ_{air}
τ_{air}, C_h
Droplet impingement
$\mathbf{U}_{droplet}$, β
CHT3D anti-icing
Coupled iteration
Multilayer heat conduction
Heat load
Wall temperature
Water film runback and phase transition

Figure 5

(a)

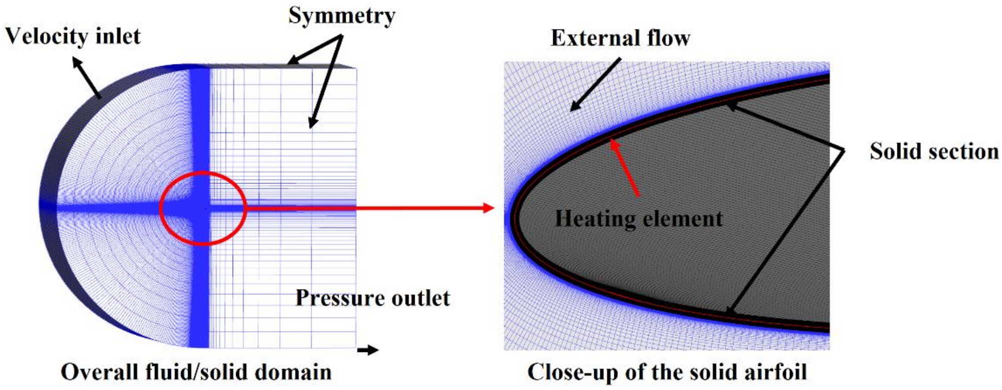
Symmetry
Velocity inlet
External flow
Solid section
Heating element
Pressure outlet
Overall fluid/solid domain
Close-up of the solid airfoil

(b)

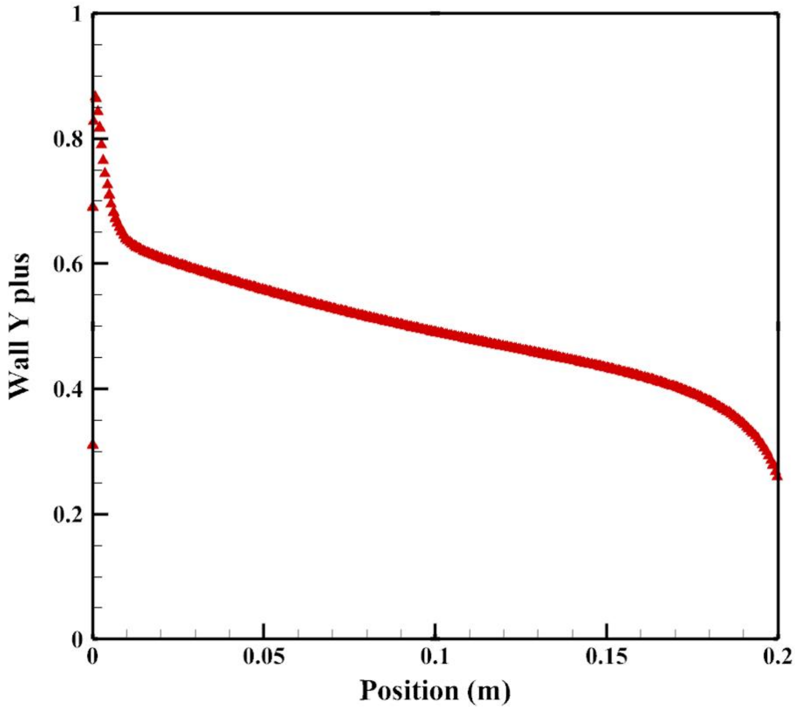
Wall Y plus
Position (m)
0
0.2
0.4
0.6
0.8
1
0.05
0.1
0.15
0.2

Figure 6

(a)

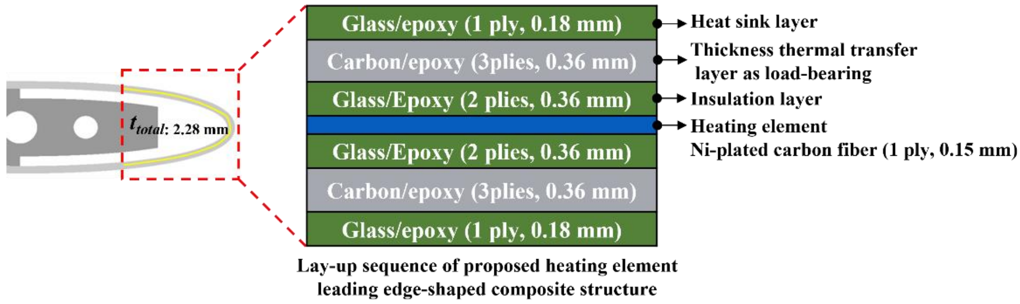

Glass/epoxy (1 ply, 0.18 mm)
Carbon/epoxy (3plies, 0.36 mm)
Glass/Epoxy (2 plies, 0.36 mm)
Glass/Epoxy (2 plies, 0.36 mm)
Carbon/epoxy (3plies, 0.36 mm)
Glass/epoxy (1 ply, 0.18 mm)
Heat sink layer
Thickness thermal transfer layer as load-bearing
Insulation layer
Heating element
Ni-plated carbon fiber (1 ply, 0.15 mm)
t_{total}: 2.28 mm
Lay-up sequence of proposed heating element leading edge-shaped composite structure

(b)

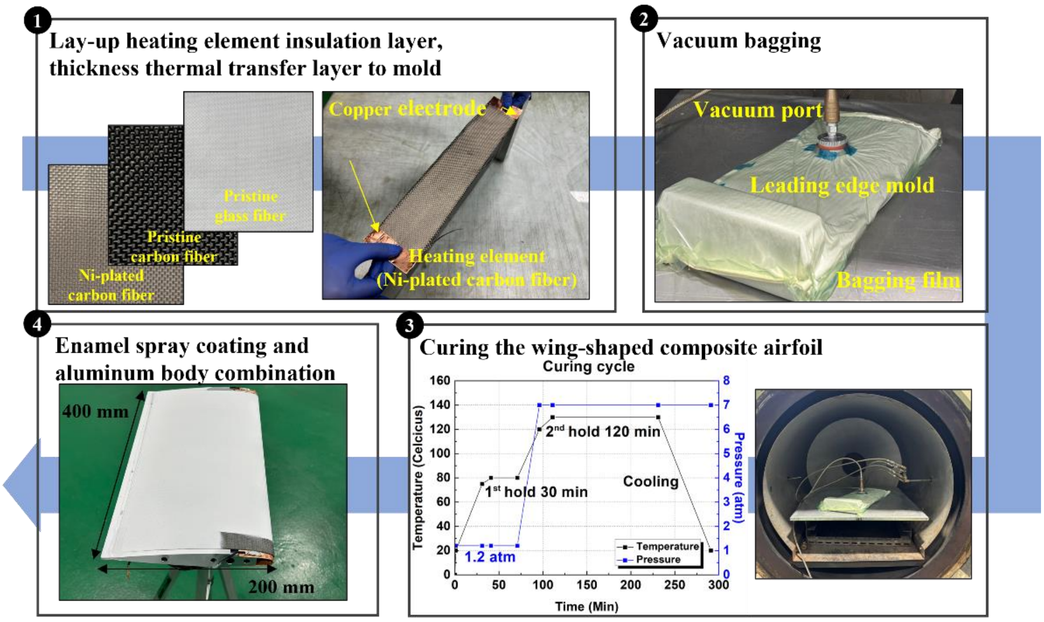

1
Lay-up heating element insulation layer, thickness thermal transfer layer to mold
Pristine glass fiber
Pristine carbon fiber
Ni-plated carbon fiber
Copper electrode
Heating element (Ni-plated carbon fiber)
2
Vacuum bagging
Vacuum port
Leading edge mold
Bagging film
3
Curing the wing-shaped composite airfoil
Curing cycle
2nd hold 120 min
1st hold 30 min
Cooling
1.2 atm
Temperature
Pressure
Temperature (Celcicus)
Pressure (atm)
Time (Min)
4
Enamel spray coating and aluminum body combination
400 mm
200 mm

Figure 7

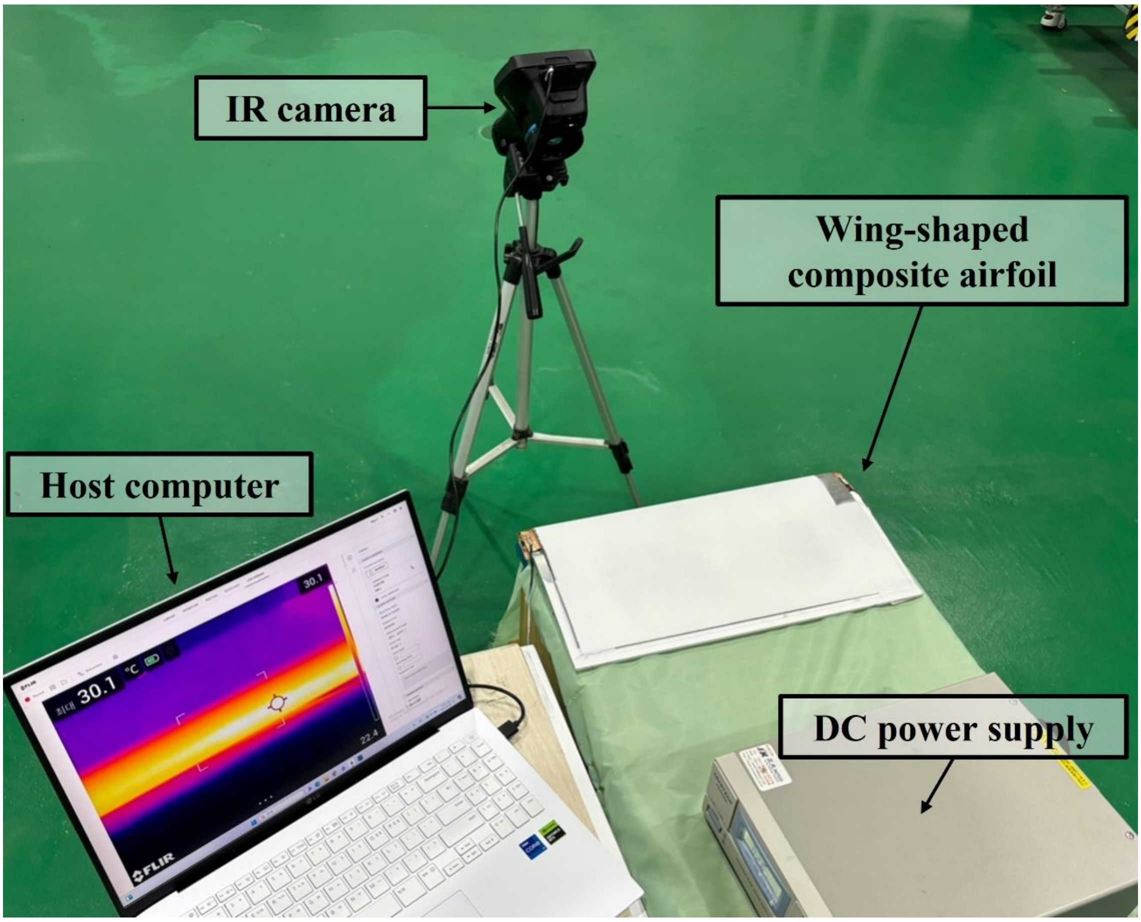
IR camera
Wing-shaped composite airfoil
Host computer
DC power supply
30.1
°C
22.4
FLIR
Figure 8

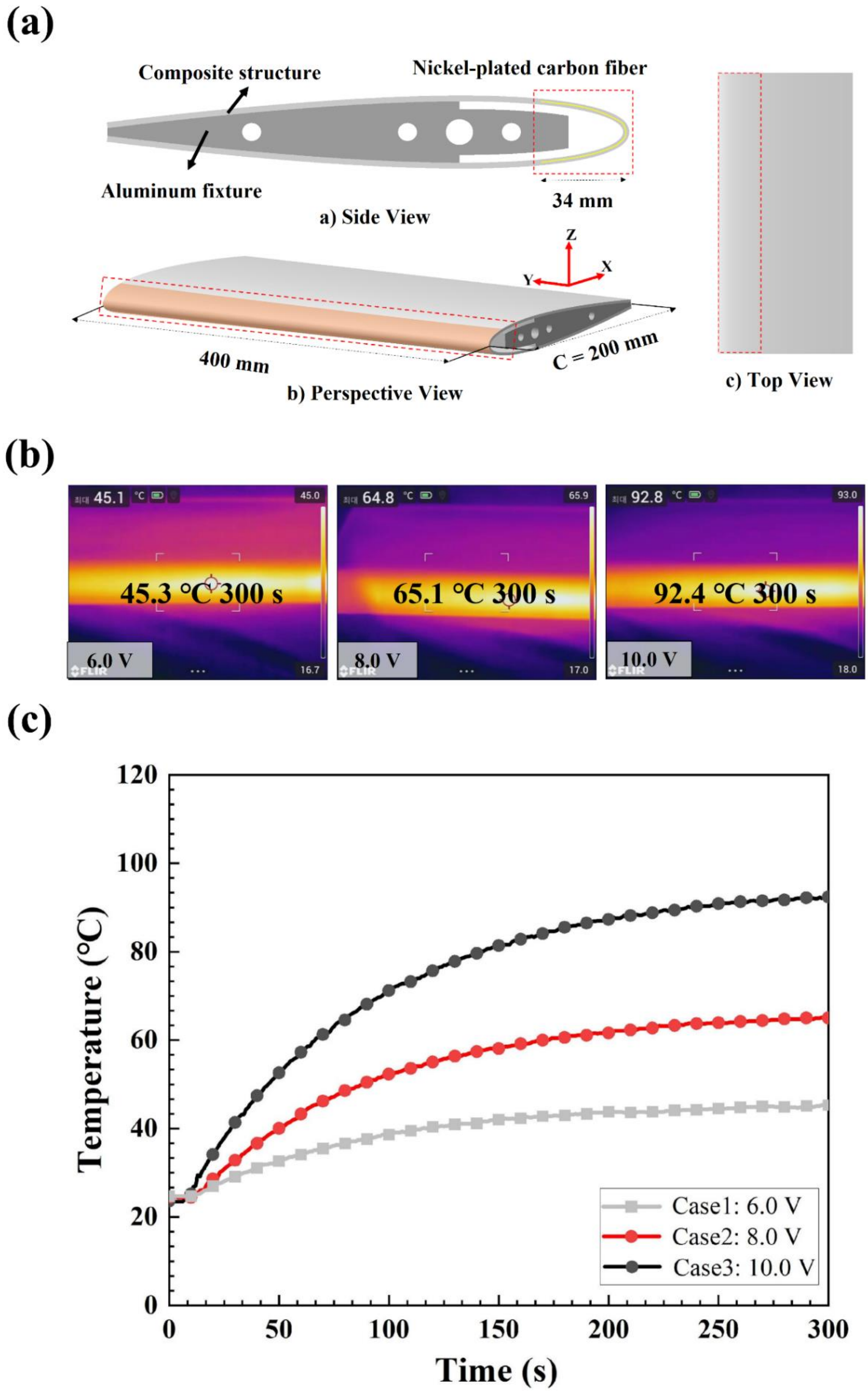

(a)
Composite structure
Nickel-plated carbon fiber
Aluminum fixture
34 mm
a) Side View
Z
Y
X
400 mm
C = 200 mm
b) Perspective View
c) Top View
(b)
45.3 °C 300 s
6.0 V
65.1 °C 300 s
8.0 V
92.4 °C 300 s
10.0 V
(c)
Temperature (°C)
Time (s)
Case1: 6.0 V
Case2: 8.0 V
Case3: 10.0 V

Figure 9

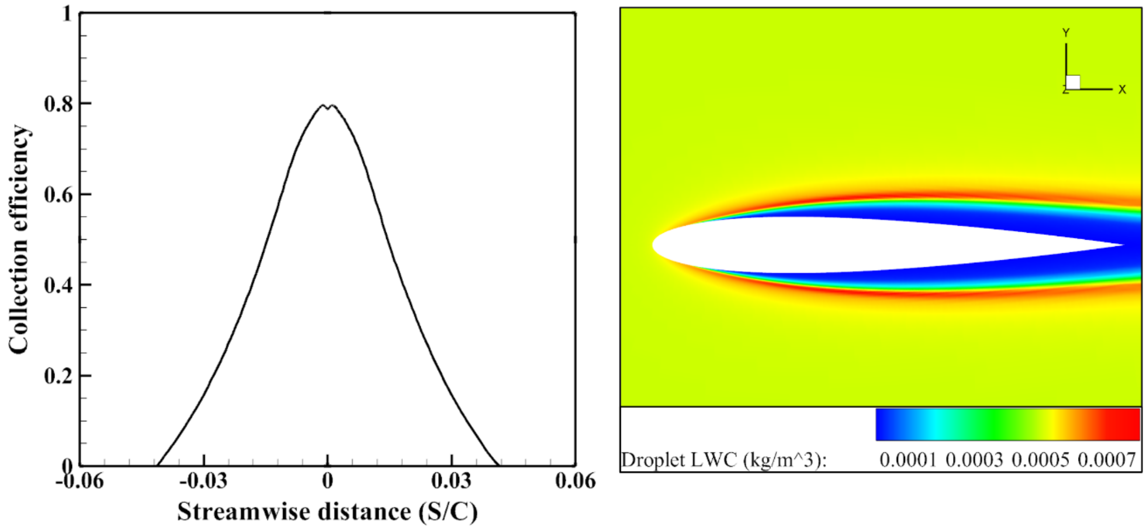

Collection efficiency
Streamwise distance (S/C)
1
0.8
0.6
0.4
0.2
0
-0.06
-0.03
0
0.03
0.06
Y
Z
X
Droplet LWC (kg/m^3):
0.0001 0.0003 0.0005 0.0007

Figure 10

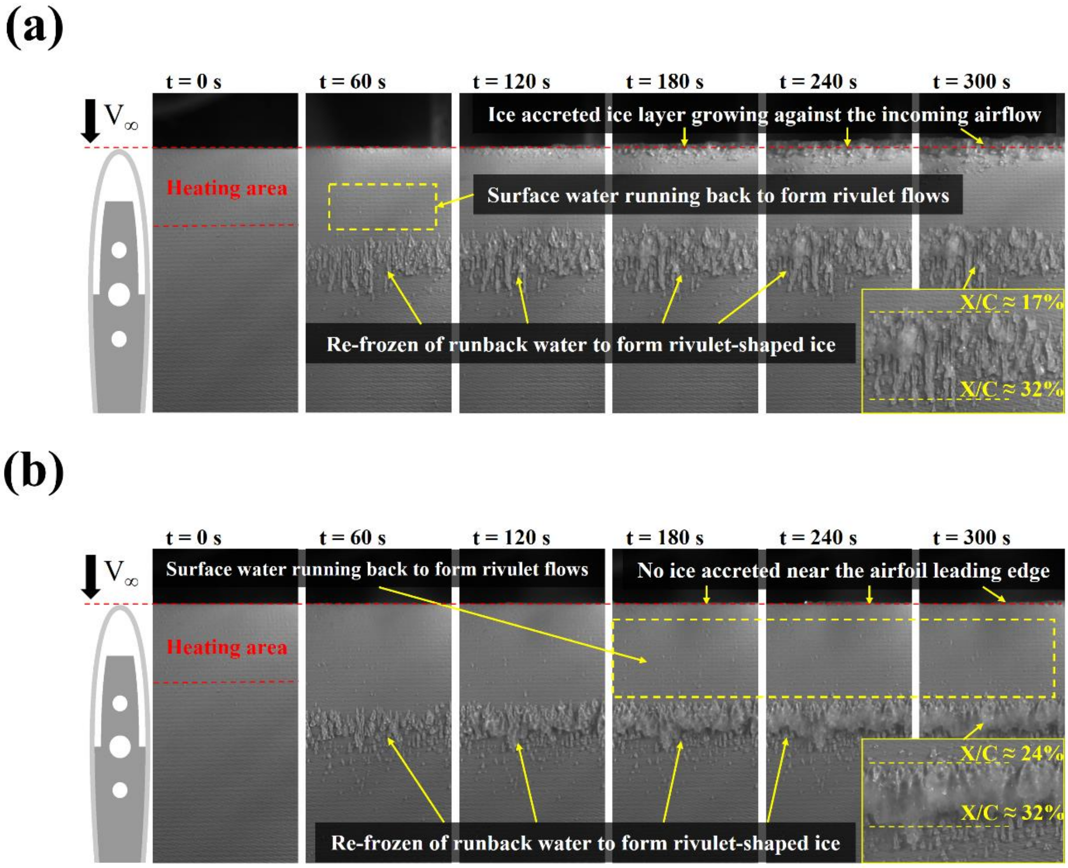
(a)
t = 0 s
t = 60 s
t = 120 s
t = 180 s
t = 240 s
t = 300 s
V∞
Ice accreted ice layer growing against the incoming airflow
Heating area
Surface water running back to form rivulet flows
X/C ≈ 17%
Re-frozen of runback water to form rivulet-shaped ice
X/C ≈ 32%
(b)
t = 0 s
t = 60 s
t = 120 s
t = 180 s
t = 240 s
t = 300 s
V∞
Surface water running back to form rivulet flows
No ice accreted near the airfoil leading edge
Heating area
X/C ≈ 24%
X/C ≈ 32%
Re-frozen of runback water to form rivulet-shaped ice

Figure 11

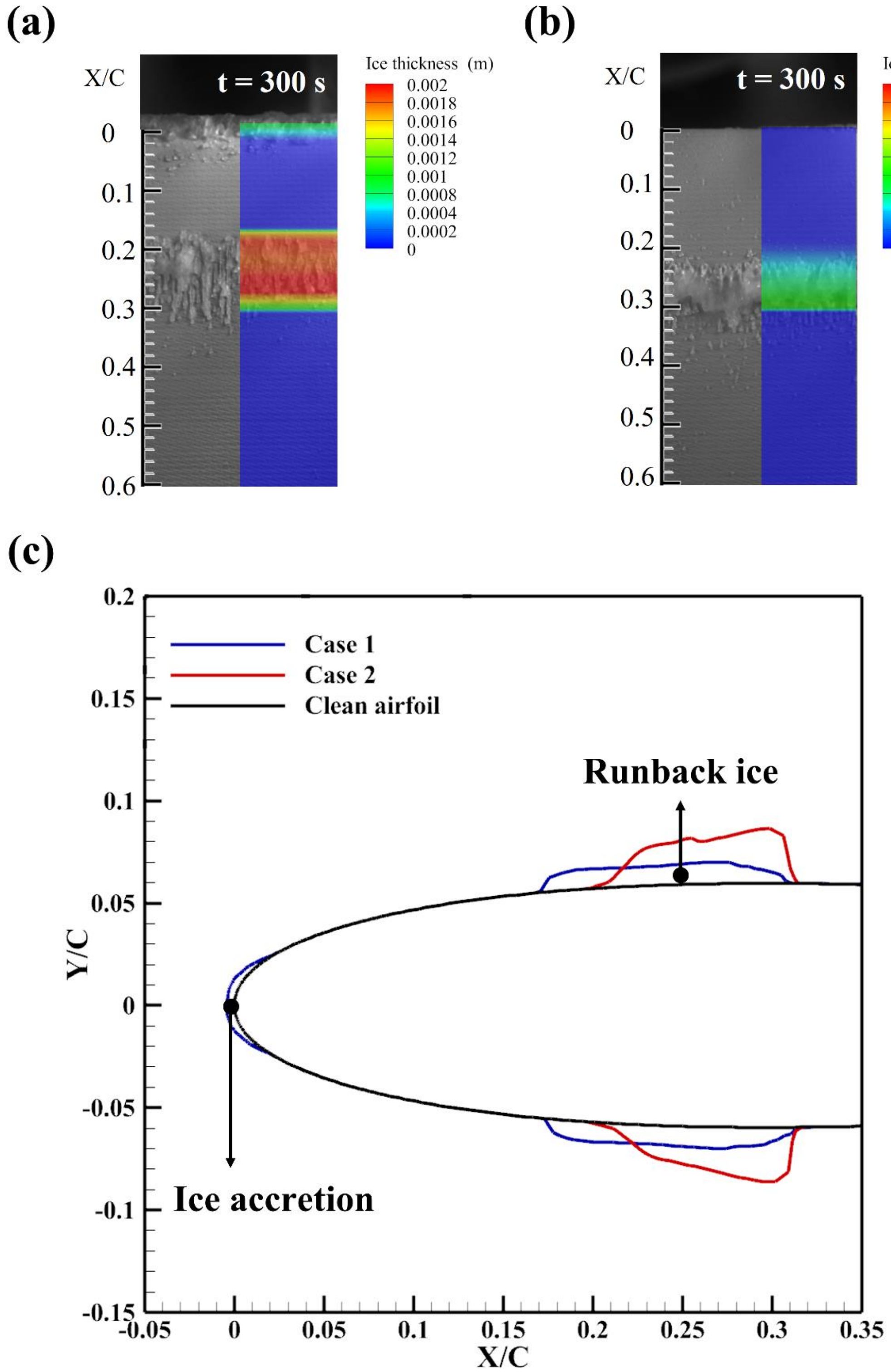
(a)
X/C
t = 300 s
Ice thickness (m)
0.002
0.0018
0.0016
0.0014
0.0012
0.001
0.0008
0.0004
0.0002
0
0
0.1
0.2
0.3
0.4
0.5
0.6
(b)
X/C
t = 300 s
Ice thickness (m)
0.002
0.0018
0.0016
0.0014
0.0012
0.001
0.0008
0.0004
0.0002
0
0
0.1
0.2
0.3
0.4
0.5
0.6
(c)
Case 1
Case 2
Clean airfoil
Runback ice
Ice accretion
Y/C
0.2
0.15
0.1
0.05
0
-0.05
-0.1
-0.15
-0.05
0
0.05
0.1
0.15
0.2
0.25
0.3
0.35
X/C

Figure 12

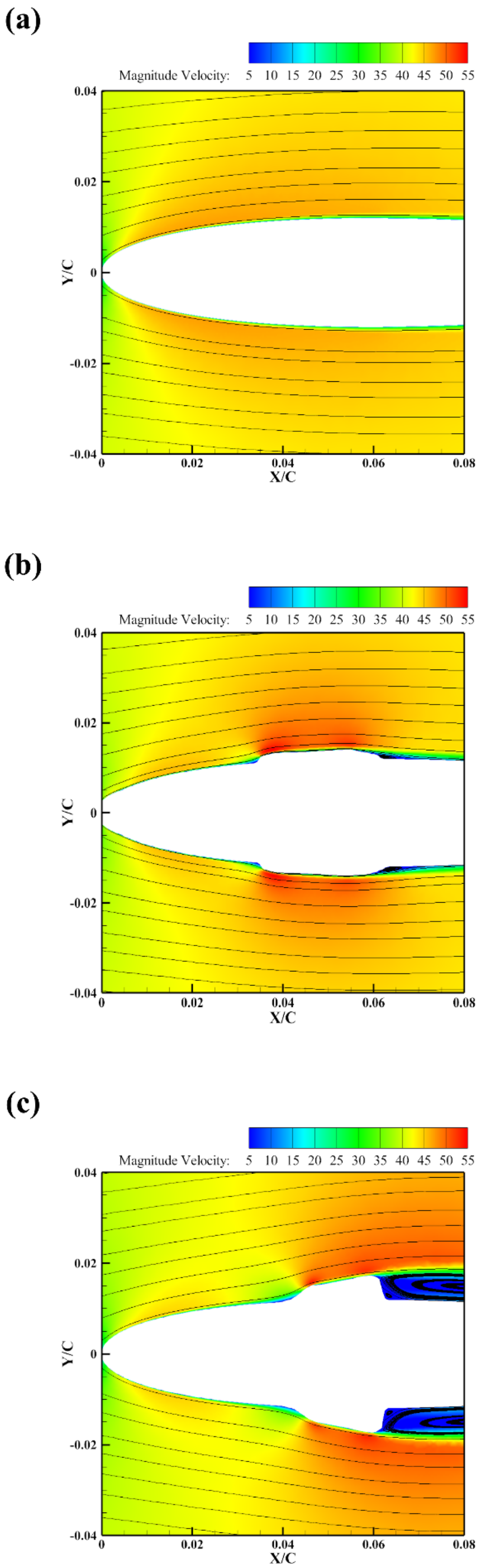
(a)
Magnitude Velocity: 5 10 15 20 25 30 35 40 45 50 55
Y/C
0.04
0.02
0
-0.02
-0.04
X/C
0
0.02
0.04
0.06
0.08
(b)
Magnitude Velocity: 5 10 15 20 25 30 35 40 45 50 55
Y/C
0.04
0.02
0
-0.02
-0.04
X/C
0
0.02
0.04
0.06
0.08
(c)
Magnitude Velocity: 5 10 15 20 25 30 35 40 45 50 55
Y/C
0.04
0.02
0
-0.02
-0.04
X/C
0
0.02
0.04
0.06
0.08

Figure 13

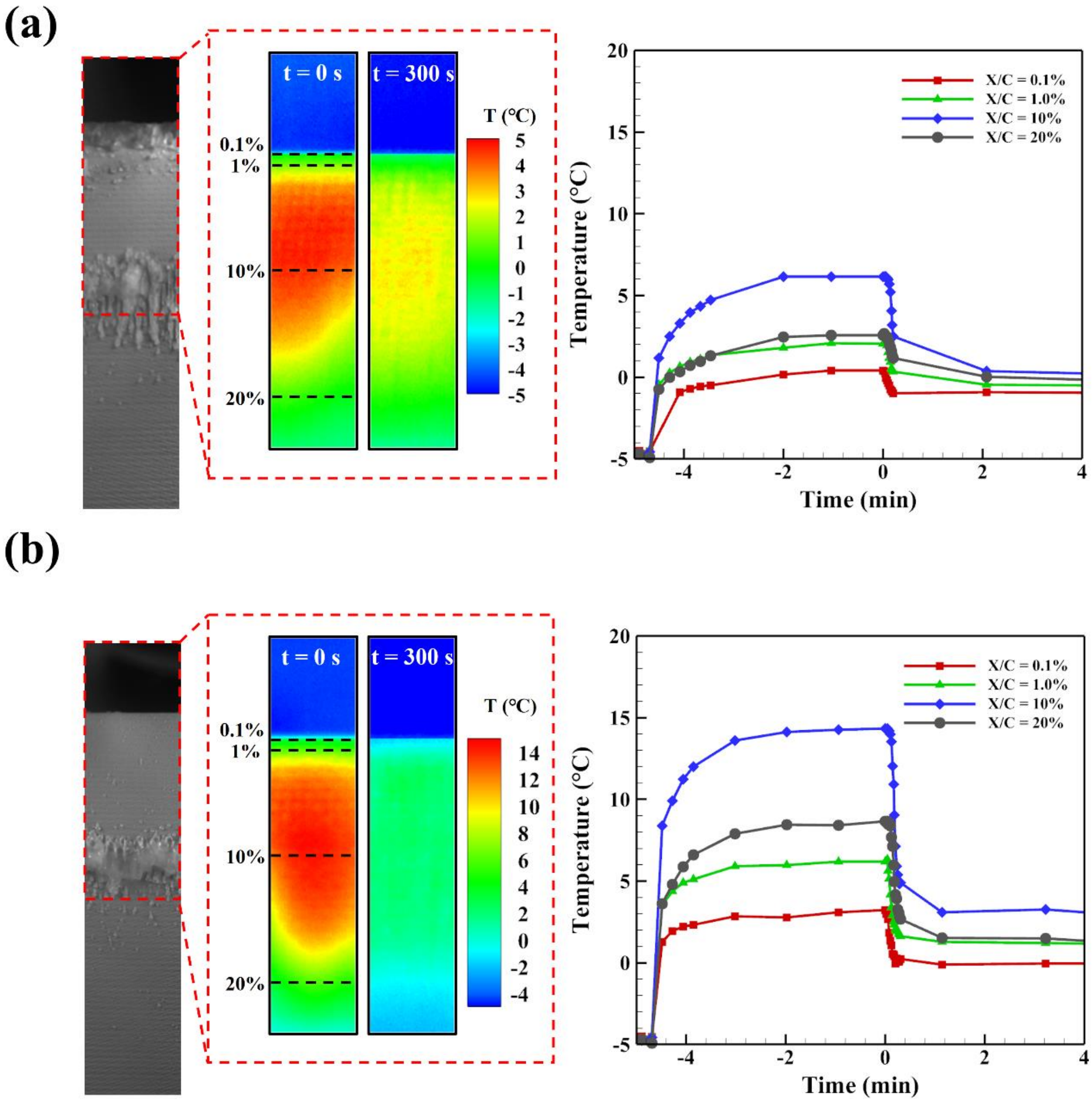
(a)
t = 0 s
t = 300 s
0.1%
1%
10%
20%
T (°C)
5
4
3
2
1
0
-1
-2
-3
-4
-5
X/C = 0.1%
X/C = 1.0%
X/C = 10%
X/C = 20%
Temperature (°C)
Time (min)
(b)
t = 0 s
t = 300 s
0.1%
1%
10%
20%
T (°C)
14
12
10
8
6
4
2
0
-2
-4
X/C = 0.1%
X/C = 1.0%
X/C = 10%
X/C = 20%
Temperature (°C)
Time (min)

Figure 14

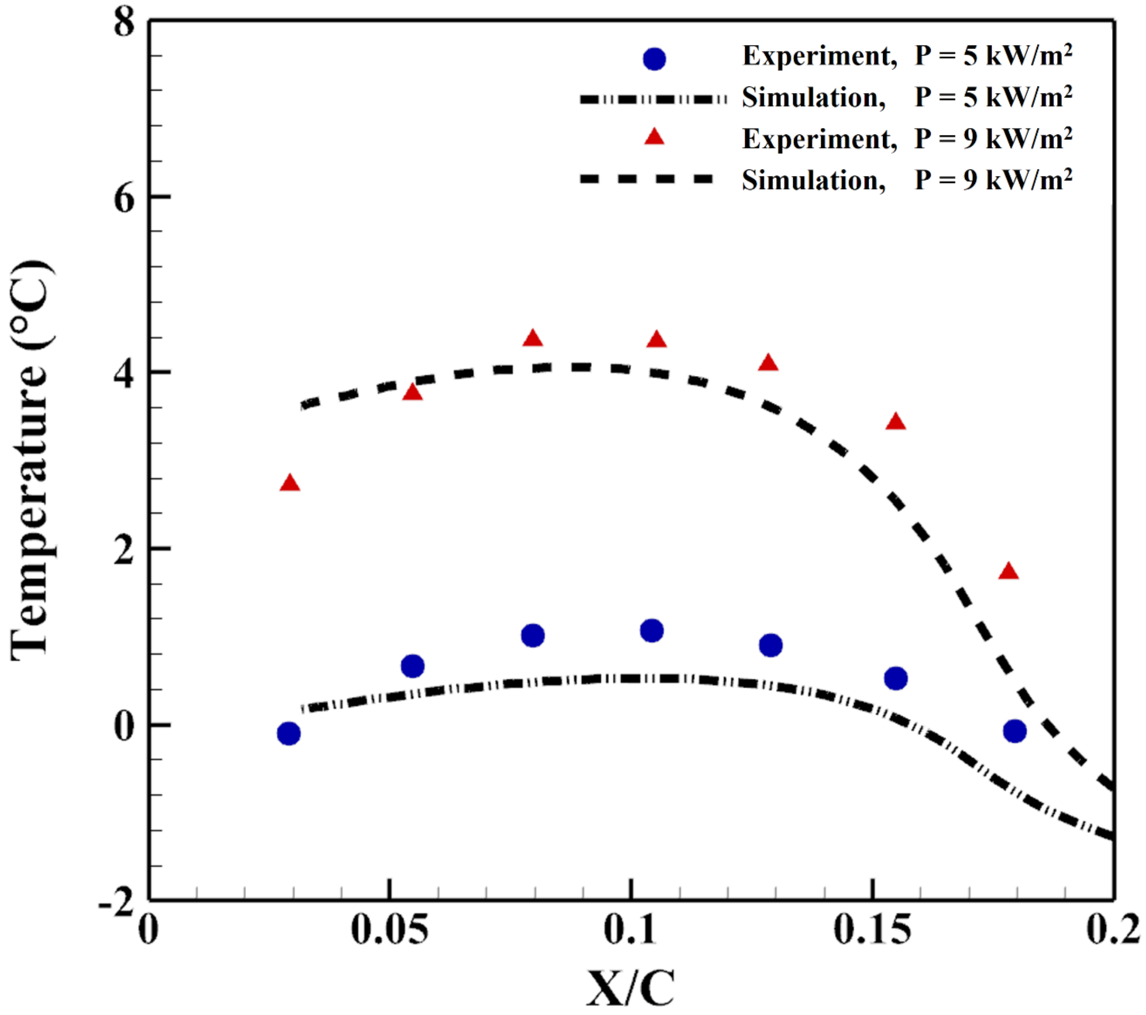
Experiment, P = 5 kW/m²
Simulation, P = 5 kW/m²
Experiment, P = 9 kW/m²
Simulation, P = 9 kW/m²
Temperature (°C)
X/C
8
6
4
2
0
-2
0
0.05
0.1
0.15
0.2

Figure 15

Tables

Table 1. Comparison of icing wind tunnel tests with composite experimental models as reported in the literature survey.

Authors	Materials	Icing wind tunnel test conditions			
		Airfoil models	T (°C)	V (m/s)	LWC (g/m^3)
Gao et al. (2019) [12]	Polymer-composite	DU96-W-180	-10	40.0	0.30–3.00
Jasinski et al. (1997) [13]	Carbon fiber	S809	-10	65.2	0.10
Wang et al. (2024) [14]	Glass-fiber-reinforced plastic	DU97	-5	10.0	3.20
Lin et al. (2023) [15]	T300-carbon-fiber-reinforced plastic	NACA0018	-5, -10, -15	10.0	0.10–5.00
Yan et al. (2018) [16]	Carbon fiber	MJI Mavic Pro	-12	5.0	1.50
Gao et al. (2019) [17]	Polymer-composite	DU91-W2-250	-5	40.0	1.10
Wang et al. (2024) [18]	Carbon-/glass-fiber-reinforced plastic	SC0710	-10	6.1–16.2	0.50
Liu et al. (2023) [19]	Glass-fiber-reinforced plastic	NACA0018	-5, -10	5.0–15.0	0.50–1.00
Endres et al. (2016) [20]	Glass-fiber-reinforced plastic	NACA0012	-3, -10, -15, -20	40.0	1.30, 2.00
Müller et al. (2023) [21]	Carbon-/glass-fiber-reinforced plastic	21×13 EL	-5	25.0	0.44
Karpen et al. (2022) [22]	Carbon-fiber-reinforced plastic	1345s	0, -10	2.2	0.78
Wallisch et al. (2022) [23]	Glass-fiber-reinforced plastic	RG-15	-2, -5, -10, -15	25.0	0.44
Mohseni et al. (2013) [24]	E-765 epoxy/fiber glass prepreg	NACA0021	-17	27.7	0.84, 1.05
Hasan et al. (2021) [25]	S2-glass/FM906 lamina	Specimen	-5, -6	12.7	1.60
Present work	Nickel-plated carbon fiber Carbon-/glass-fiber-reinforced plastic	NACA0012	-5	40.0	0.50

Table 2. Compositions of pristine and nickel-plated carbon fabric determined by EDS.

Samples	Weight percentage (wt. %)/atomic percentage (at. %)		
	Ni	Cu	C
Pristine carbon fiber	0.00/0.00	0.00/0.00	100/100
Nickel-plated carbon fiber	75.98/63.04	18.39/14.10	5.64/22.86

Table 3. h_{r+c} values of the heating elements at an applied voltage of 1.5 V.

Materials	V_0 (V)	I_c (A)	T_0 (℃)	T_m (℃)	h_{r+c} (W/℃)
Pristine carbon fiber	1.50	0.42	26.00	33.30	0.09
Ni-plated carbon fiber	1.50	4.30	24.60	88.60	0.10

Table 4. Test conditions for icing wind tunnel experiments of wing-shaped composite models at various power densities.

Cases	Temperature (K)	Velocity (m/s)	LWC (g/m^3)	MVD (μm)	AoA (deg)	Power density (W/m^2)
Case 1	268.15	40	0.5	20	0	5000
Case 2	268.15	40	0.5	20	0	9000

Table 5. NACA 0012 ice accretion grid mesh features according to grid convergence test.

Mesh feature	Finer mesh	Initial mesh	Coarser mesh
Point on upper and lower side	702	491	350
Leading edge spacing [mm]	0.054	0.077	0.112
Trailing edge spacing [mm]	0.490	0.610	0.871
Points on velocity inlet	600	428	305

Table 6. Surface temperature of the wing-shaped composite at various applied voltages.

Voltage (V)	Current (A)	Power density (kW/m^2)	Maximum temperature T_m (°C)	Duration time (s)
6.0	7.22	1433.3	45.3	600
8.0	9.76	2600.0	65.0	600
10.0	12.20	4066.7	92.4	600